# Domain convexification: A simple model for invasion processes

David Martin-Calle and Olivier Pierre-Louis ⓞ

*Institut Lumière Matière, Université de Lyon, Université Claude Bernard Lyon 1, CNRS UMR5306,
Campus de la Doua, F-69622 Villeurbanne, France*

We propose an invasion model where domains grow up to their convex hulls and merge when they overlap. This model can be seen as a continuum and isotropic counterpart of bootstrap percolation models. From numerical investigations of the model starting with randomly deposited overlapping disks on a plane, we find an invasion transition that occurs via macroscopic avalanches. The disk concentration threshold and the width of the transition are found to decrease as the system size is increased. Our results are consistent with a vanishing threshold in the limit of infinitely large system sizes. However, this limit could not be investigated by simulations. For finite initial concentrations of disks, the cluster size distribution presents a power-law tail characterized by an exponent that varies approximately linearly with the initial concentration of disks. These results at finite initial concentration open novel directions for the understanding of the transition in systems of finite size. Furthermore, we find that the domain area distribution has oscillations with discontinuities. In addition, the deviation from circularity of large domains is constant. Finally, we compare our results to experimental observations on de-adhesion of graphene induced by the intercalation of nanoparticles.

## I. INTRODUCTION

Invasion transitions, where domains invade the entire space, are found in many two-dimensional systems [1,2] ranging from phase transitions in magnets to de-adhesion transitions and spreading of species in ecology models. In this paper, we propose a simple two-dimensional model for isotropic invasion in continuous space where each domain grows up to its convex hull, thereby invading the concave parts along its periphery. If this growth process up to the convex hull, hereafter denoted as convexification, leads to overlapping with other domains, then these domains are merged. Merging of domains produces new concavities, leading to additional domain growth.

A schematic of the model starting with randomly deposited overlapping disks on a plane is shown in Fig. 1. The initial domains are the disks. We apply iteratively convexification and merging. Since the disks are convex, they are identical to their convex hull and the first convexification of each disk does not change the disks. The first merging groups the disks in clusters of mutually overlapping disks. They lead to clusters with different colors on Fig. 1(a). The convexification of these clusters leads to convex domains, as shown in Fig. 1(b). When these domains overlap, they are merged. Hence, the blue and green domains in Fig. 1(b) are merged, leading to a larger domain in Fig. 1(c). This iterative convexification and merging process is stopped when no new merging can be performed, as in Fig. 1(d). Our numerical investigation of this model in large systems shows that it exhibits an invasion transition as the initial density of disks is increased.

Our model constitutes a continuous and isotropic counterpart of the bootstrap percolation model [3–5]. Bootstrap percolation models are on-lattice models where domains grow irreversibly at sites that have a sufficient number of bonds with the existing domains. For a large enough threshold in the number of bonds (2 for the square lattice), and starting from random initial conditions with a given initial density of occupied sites, the domains grow up to a final state which is either a set of disconnected domains with a finite domain density, or a single domain that has invaded the whole system. A transition between these two regimes occurs at a finite initial density of occupied sites for systems with a finite size. However, this finite initial density threshold is a finite-size effect, and, in the limit of very large systems, the threshold of the transition occurs at vanishing initial densities [6]. The convergence to the limit of large system size in bootstrap percolation is notoriously slow (the largest simulations reported in Ref. [7] on a square lattice with $(2.2 \times 10^5)^2$ sites are still far from the asymptotic behavior of Ref. [6]). Our simulations show that the transition threshold of our convexification model decreases with increasing system size. Our numerical evidence (with up to $10^8$ disks) is insufficient to conclude whether the threshold vanishes for very large sizes. However, in the range of system sizes that we have explored, we find that the threshold and the width of the transition decrease when the system size increases.

Moreover, the bootstrap percolation transition is known to occur in a discontinuous way via a macroscopic avalanche when increasing the initial density of occupied sites [8–10]. Such a discontinuity has attracted much attention in the literature. Other percolation models were also found to exhibit strongly discontinuous transitions, often called explosive percolation [11,12]. Macroscopic avalanches have also been observed in the depinning transition of the low-temperature random field Ising model [13–15]. In both bootstrap percolation and depinning transitions, the discontinuous character of macroscopic avalanches is associated with strong finite-size effects that are rooted in rare events [7,15]. For large-enough
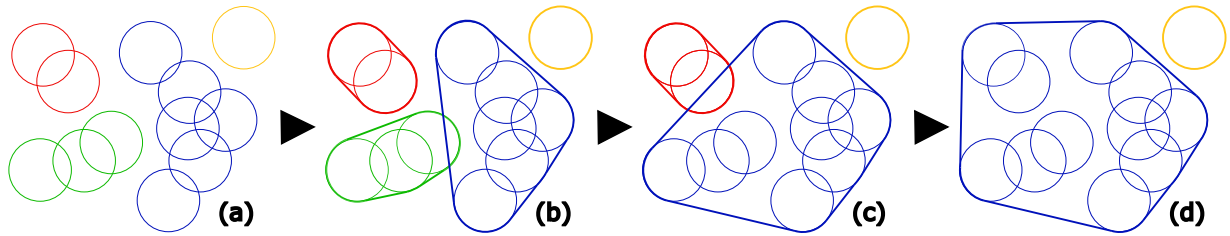
FIG. 1. Schematic of the iterative convexification and merging process. The initial state with a set of overlapping disks is shown in (a). The process is repeated as long as merging is possible (see text for details). We analyze the final state at the end of this process. The final state shown in (d) consists of two clusters: one cluster with 11 disks, and one cluster with 1 disk.

systems, we also observe that the transition takes the form of a macroscopic avalanche that can be triggered by a microscopic perturbation, for example, the addition of a single disk to the initial condition.

The bootstrap percolation and depinning transitions occur in simple paradigmatic models that are expected to catch the essence of a wide variety of physical phenomena, from the jamming transition to crack propagation. In like manner, we expect our model to pertain to a large class of systems where invasion transitions can be observed, due to our model's isotropic lattice-free character.

A first class of phenomena that may be described by the convexification model is line-tension induced growth of two-dimensional domains with random impurities or defects. In contrast to the random field Ising model, the randomness then only originates in the initial condition: we assume that one type of magnetization is imposed in some randomly placed disk-shaped zones. Outside these zones, the interface between the two types of magnetization moves freely, and is subject to standard motion by curvature driven by line tension [1,2]. Hence, these interfaces straighten and build the convex hull of the initial zones. Due to the equivalence between lattice gas models and the Ising model [16], this process also describes the dynamics of adsorption of a monolayer of molecules (or particles) with short-range attractive interactions on a flat substrate in the presence of localized defects or impurities which enforce the initial coverage of some circular zones. Another similar system is the imbibition in a Hele-Shaw geometry [17–19] with strongly wetting defects, a geometry that mimics imbibition of porous media.

A second class of physical phenomena that could be described by domain convexification is third-body induced de-adhesion transitions. These transitions are relevant to friction and its coupling with wear, but also to intercalation of particles, molecules, or atoms inside layered materials such as graphite [20–22]. A simple view of the de-adhesion transition is the following. When particles are intercalated in the contact zone between two bodies, each particle leads to a local de-adhesion zone around it. When these zones overlap, the concave parts of their periphery can be rounded, leading to a growth of the de-adhesion zone. This growth can lead to new overlap with other de-adhesion zones, and the growth of de-adhesion zones occurs again. When the density of particles is large enough, this leads to de-adhesion of the full contact zone. This generic phenomena has been observed in the case of de-adhesion of graphene with intercalated nanoparticles [23]. One advantage of using a two-dimensional material

like graphene is the possibility of imaging the detailed geometry of detachment zones induced by nanoparticles. In these experiments, a de-adhesion transition is observed when the density of intercalated nanoparticles or the rigidity of the membrane are increased. The convexification model appears as a idealization of this process which assumes that detachment zones simply grow up to the convex hull of the detachment zones that would be induced by each particle independently. The physics of de-adhesion is expected to be more complex than this simple model, since the de-adhesion zones might grow only partially towards their convex hull, or grow to a different shape. Also, other features are expected depending on the precise adhesion properties and elastic properties of the system, such as wrinkles and conical singularities [23–26]. However, we hope to catch some generic features of this phenomenon with our simple model, and below we report a quantitative analysis of the intercalation-induced graphene de-adhesion observed in experiments.

The convexification model could also be relevant for the modeling of invasion in population dynamics. Indeed, most models for the invasion of a population in continuous space are based on ingredients that lead to finite propagation speed for straight fronts [27–30]. Our model proposes a different paradigm, and suggests a scenario of species invasion with no net growth for straight fronts. Instead, the invading domain could grow only via the process of convexification. A simple mechanism for this process is straight-line traveling of individuals between different points of the domain, and merging of domains where individuals meet (due, e.g., to breeding). Since the ensemble of straight lines starting and ending in a domain cover its convex hull, we then obtain the convexification model. Our results can be translated as the following statement for population dynamics: above a critical initial density of randomly placed domains where the species, the whole system will be invaded. Our results suggest that, starting from a randomly scattered population that has no propensity to spread, invasion and merging into a single group could be triggered by the motion of individuals in straight lines within their own population domain.

Finally, we point out the possible relevance of our model for classification and clustering of complex sets of points or domains in the plane. In statistics and data analysis, one of the elementary questions that is at the root of many clustering algorithms is the linear separability of sets of points [31–33]. In our two-dimensional plane, two sets of points or two

domains of the plane are said to be linearly separable if they can be separated by a straight line. Since two disjoint convex clusters can always be separated by a straight line, they are linearly separable from each other. The convex hull of a set of points is actually a standard tool for studying linear separability [34]. Moreover, the straight line that maximizes the distance from the points of two clusters is called the maximum margin hyperplane, and its distance to the closest points is called the maximum margin [35,36]. It is clear that in our model two clusters will not merge if the maximum margin between their disk centers is larger than the disk radius $r_d$. As a consequence, the condition of linear separability of clusters with maximum margins larger than $r_d$ is equivalent to our condition for stopping the convexification procedure. In other words, the invasion transition corresponds to the threshold above which it is not possible to separate linearly clusters of randomly scattered points with a maximum margin larger than $r_d$.

A closely related subject is the separation of objects in images using their convex hulls [37]. As discussed in Refs. [38,39] the construction of convex hulls can be obtained by the propagation of the boundary of the domain with a modified motion-by-curvature equation governing the normal velocity $v_n$,

$$v_n = -\min(\kappa, 0), \qquad (1)$$

where $\kappa$ is the local curvature (positive for convex domains). This equation is actually similar to the models discussed above for the growth of magnetization models or monolayers from initial defects.

In the following, we will start with a detailed description of the model and its numerical analysis in Sec. II.

The simulation results are reported in Sec. III. We discuss the main features of the invasion transition in Sec. III A, namely, macroscopic avalanches and the decrease of the threshold and width of the transition as the system size increases. In Sec. III B, we introduce an order parameter which measures the average fraction of the system that is not invaded. In Secs. III C and III D, we discuss the domain size and area distributions. For finite concentrations of initial disks, the tails of the domain size distribution are found to present a power-law behavior with a continuously varying exponent. Moreover, the domain area distribution is found to have oscillations accompanied by discontinuities. We then report shortly on domain shapes in Sec. III E. We find that the average shape of large domains presents a constant deviation from a circular shape.

Further discussions and analysis of the transition are reported in Sec. IV. After a comparison with on-lattice bootstrap percolation in Sec. IV A, we distinguish two regimes for the transition: a first regime at small concentrations leading to a behavior that is similar to the asymptotic regime of bootstrap percolation discussed in Sec. IV B, and a second regime at finite concentrations discussed in Sec. IV C.

In Sec. V, we compare our results with experiments where the intercalation of nanoparticles leads to the de-adhesion of graphene [23]. We find that experimental results can be described quantitatively with our model assuming a finite-size effect involving around 200 particles.

Finally, we provide a brief summary of our results in Sec. VI.

## II. MODEL

### A. Model ingredients and definitions

We consider a two-dimensional system. The initial condition consists of randomly placing $N_d$ disks of radius $r_d$ in a two-dimensional system of area $A_{\text{syst}}$. More precisely, the centers of the disks are chosen from a continuous uniform probability distribution on the system area. The concentration of disks is characterized by the dimensionless concentration

$$C = \frac{N_d \pi r_d^2}{A_{\text{syst}}}. \qquad (2)$$

In the following, a *cluster* will denote one of the groups of disks resulting from the convexification process. In addition, *a domain* will denote the region of the plane that corresponds to the convex hull of a cluster.

The initial domains correspond to the zones of the plane that are covered by one disk, or several overlapping disks. The overlapping disks belonging to one initial domain in the plane correspond to the percolation clusters of continuum disk percolation [40]. The percolation threshold above which infinite percolation clusters exist in large systems is $C_p \approx 1.128$ [41]. The average area fraction not covered by the disk percolation domains is [23]

$$\Phi_p(C) = e^{-C}. \qquad (3)$$

This relation is valid in systems of large size when $A_{\text{syst}} \gg \pi r_d^2$, so that the effect of boundary conditions can be neglected.

Starting from this random initial condition with disk percolation clusters, we apply the following iterative convexification procedure. First, we consider that any domain grows up to its convex hull; this is the convexification step. Then, domains that overlap are merged; this is the merging step. We apply iteratively these two steps up to the situation where no new merging occurs in the merging step. A schematic of the convexification process is shown in Fig. 1.

Such an iterative algorithm aims at mimicking the invasion processes that were discussed in the Introduction. Note that the precise dynamics of the interface that describes how the domain boundary grows up to the convex hull in the convexification step is not described. However, the final state composed of a set of disconnected convex domains is clearly unique, and this final state is the focus of our analysis.

More precisely, we wish to investigate the dependence of the final state on the two dimensionless numbers that govern the problem: the disk concentration $C$, and the normalized system size

$$\bar{A}_{\text{syst}} = \frac{A_{\text{syst}}}{\pi r_d^2}. \qquad (4)$$

We have performed numerical simulations where the variation of $C$ is obtained by adding disks one by one so as to increase $N_d$ for a fixed $\bar{A}_{\text{syst}}$. Once a new disk is added, we iterate convexification and merging steps in the system, and the algorithm converges to a new final state. The simulation

results reported in the following sections are performed with $C$ varied from 0 to 1 for various values of $\bar{A}_{\text{syst}}$ between $10^2$ and $10^8$.

We report simulation results with two types of boundary conditions. The first type of boundary condition, hereafter denoted as fixed boundary conditions, corresponds to a system where the centers of the disks of radius $r_d$ are placed within a circular system of radius $R_{\text{syst}}$ and area $A_{\text{syst}} = \pi R_{\text{syst}}^2$. Note that, when the center of a deposited disk is close to the edge of the system, part of this disk may lie outside the system. This leads to corrections to Eq. (3) that are negligible when $r_d \ll R_{\text{syst}}$.

We also consider the case of periodic boundary conditions in a square box of size $L_{\text{syst}} \times L_{\text{syst}}$ and area $A_{\text{syst}} = L_{\text{syst}}^2$. The investigation of periodic systems requires a careful definition of convex hulls. This definition is discussed in Appendix A.

### B. Details on the simulation algorithm

Below we provide some details about the algorithm that we have used to build the clusters. The reader who is not interested in this specific technical discussion can switch directly to Sec. III.

For each cluster, we use the Jarvis march algorithm [42] to obtain the lists containing the $N_{\text{out}}$ outlying disks that are in contact with the boundary of the domain. As shown in Fig. 2, the boundary of the domain is composed of arcs of circles that belong to the edges of the outlying disks, and segments between two outlying disks. Disks inside the cluster (i.e., not outlying) can be discarded for the computation of the merging and convexification processes.

We add disks one by one. A new disk will belong to a given cluster if the center of the new disk falls inside the fictitious convex-hull domain of the cluster that is formed by assuming disks of radius $2r_d$. Testing the contact requires the computation of $N_{\text{out}}$ tests for checking on which side of the domain boundary segments the center of the new disk is, and $N_{\text{out}}$ tests for checking if the center of the new disk is in the outlying disks.

If the new disc is in contact with no cluster, a new one-disk cluster is created. Otherwise, the new disk is merged with the first cluster with which it is found to be in contact when browsing the list of clusters.

If the new disk is a new outlying disk of the cluster with which it is merged, then the new disk is added to the list of outlying disks. In such a case the cluster domain changes and grows, and the algorithm starts testing the contact of this modified cluster with the other clusters. To test the contact between the growing cluster and the other clusters, we test the contact of each outlying disk of other clusters with the growing cluster. From this point on, at each step of convexification, the growing cluster is simultaneously merged with all the clusters that are in contact with it. Then, the new convex hull is computed, and contact tests are resumed. The growth process is iterated until no contact is found between the clusters.

To accelerate the simulations, a compartmentalization method is implemented, following Ref. [40]. The system is covered by a square grid with cells of side $2r_d$. Contact tests of a disk with a cluster are performed only if the center of
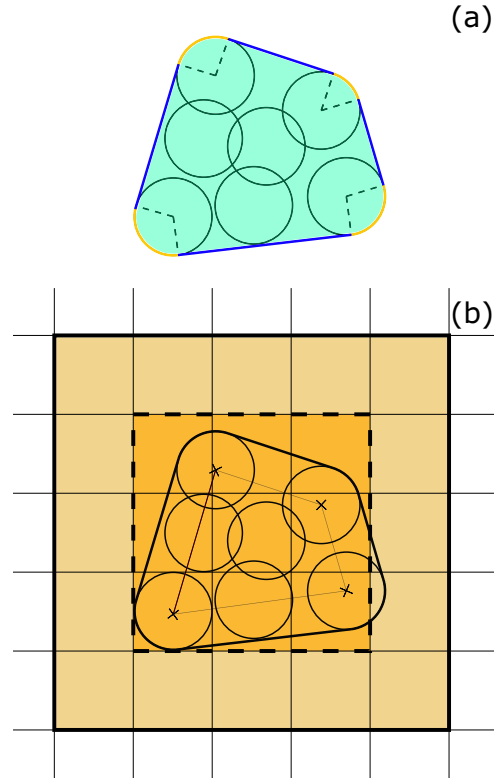


FIG. 2. Schematic of a seven-disk cluster with four outlying disks. (a) The light (green) shading represent the cluster domain. The boundary of the domain is composed of straight segments and arcs of circle. (b) Compartmentalization grid with squares of size $2r_d \times 2r_d$. A rectangle is constructed, which contains all disk centers plus one shell of grid cells (shown in lighter shading). Contact tests are performed with other disks only when their centers fall into this rectangle.

the disk belongs to the minimal rectangle of grid cells that contains the centers of the disks of the cluster plus one shell of cells, as shown in Fig. 2.

As the growing cluster becomes large, the compartmentalization method tends to be counterproductive and slows the simulations down. This happens mostly during the macroscopic avalanche at the transition. Hence, if the number of outlying disks of the growing cluster exceeds an empirically chosen value of 20, compartmentalization is not used.

### III. RESULTS

### A. Transition

A first remarkable result is obtained over each individual realization, i.e., for one given sequence of added disks, and when the system is large enough, approximately when $\bar{A}_{\text{syst}} \geqslant 10^4$. We indeed observe a sharp invasion transition with the addition of a single disk. Before this critical disk is added, the final states are composed of a distribution of finite-size domains. A zoom of a square region is shown in Fig. 3 for various concentrations $C$. As $C$ increase, the area covered by the domains increases continuously and larger domains appear gradually. However, when the critical disk is added, a macroscopic avalanche of convexification spans the whole system,
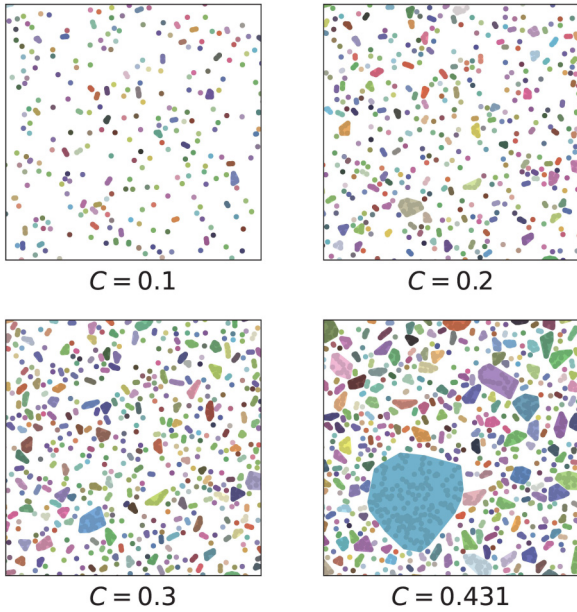
FIG. 3. Zoom on a square region ($100 r_d \times 100 r_d$) of the system, at various values of $C$. All domains are displayed, and disks inside them can be seen within the domains. The bottom right figure, at $C = 0.431$, corresponds to the state of the system just before the transition, where the addition of a single disk triggers a macroscopic avalanche leading to the invasion of the whole system. The normalized system area is $\bar{A}_{\text{syst}} = 10^5$.
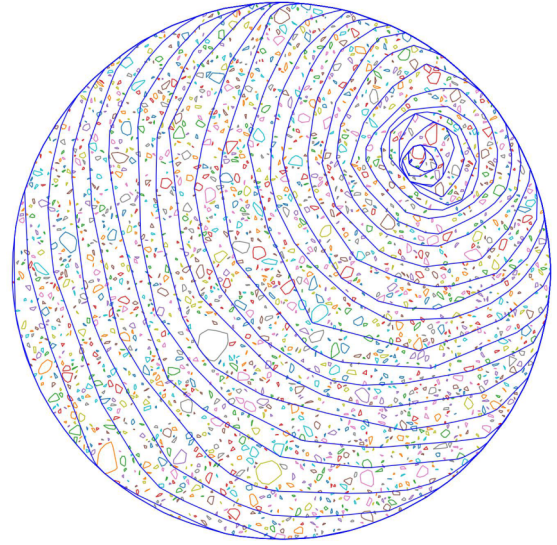


FIG. 4. Macroscopic avalanche triggered by the addition of a single disk, and invading the whole system. This corresponds to the same simulation as in Fig. 3. The growing domain is shown in blue every five iterations (where one iteration corresponds to the merging of the invading cluster with all the clusters it is in contact with). Polygons linking disk centers are shown to indicate the domains. Small clusters containing less than eight disks in their periphery are not shown. $\bar{A}_{\text{syst}} = 10^5$; the figure corresponds to the avalanche induced by the adding of the 43122th disk.
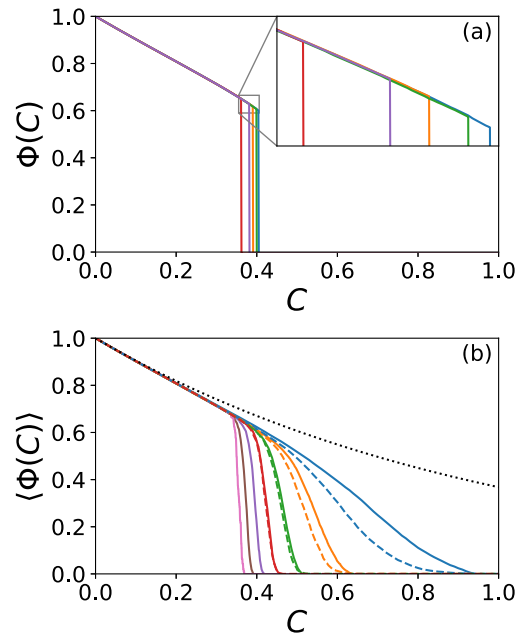
ultimately leaving only one domain that engulfs all the disks of the system. Snapshots of the convexification process when adding the critical disk are reported in Fig. 4.

The fraction $\Phi(C)$ is defined as the ratio of the system area that is not covered by the domains over the system area $A_{\text{syst}}$. In Fig. 5(a), $\Phi(C)$ is plotted for several independent realizations. As expected, we have

$$\Phi(C) < \Phi_p(C) \tag{5}$$

for any realization. Moreover, a discontinuous transition is observed in each realization. We observe that the value of $C$ where the transition occurs varies from one realization to another. Macroscopic percolation clusters are expected to be found at the percolation transition when $C \to C_p$. Since the convex hull of these macroscopic clusters spans the whole system, $C_p$ should be an upper bound for the transition. Indeed, the transitions always occurred well before the disk percolation transition in our simulations. In addition, the curve $\Phi(C)$ before the transition seems to be independent of the location of the transition; i.e., we have observed no measurable precursors or deviations before the appearance of the transition, as seen in the inset of Fig. 5(a).

An example of distribution of transition points for $\bar{A}_{\text{syst}} = 10^5$ is provided in Fig. 6(a). The average $C_c$ and the standard deviation $\Delta C_c$ of this distributions of transitions are plotted in Fig. 6(b) and 6(c) as a function of $\bar{A}_{\text{syst}}$. They both decrease with increasing system size.

In addition, the distribution of transition points also exhibits a skewness that is negative for all values of $\bar{A}_{\text{syst}}$. A plot of the skewness of the distribution is also reported in the inset of Fig. 6(c).



FIG. 5. $\Phi(C)$ as a function of the normalized disk concentration $C$. (a) $\Phi(C)$ obtained from five different simulations with a fixed system area $\bar{A}_{\text{syst}} = 10^6$ and fixed boundary conditions. The disk concentration $C$ is increased by adding disks one by one, and keeping a constant disk radius $r_d$. The inset shows a zoom of the transition region. (b) Average $\langle \Phi(C) \rangle$ for a fixed $C$. Full lines: fixed boundary conditions. Dashed lines: periodic boundary conditions. From right to left: $\bar{A}_{\text{syst}} = [10^2, 10^3, 10^4, 10^5, 10^6, 10^7, 10^8]$ averaged over $[10^3, 10^3, 10^5, 10^4, 10^3, 10^3, 60]$ realizations. Dotted line: exponential decrease of the order parameter without convexification, Eq. (3).
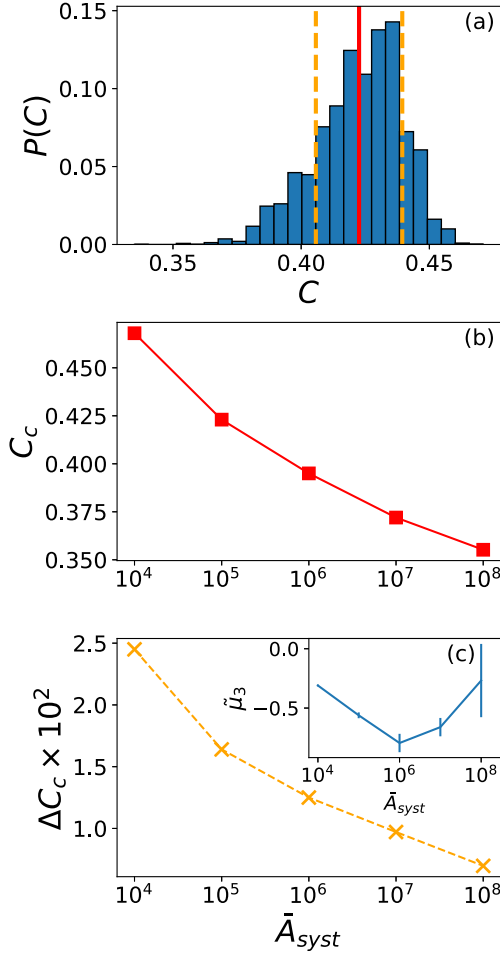
FIG. 6. Transition for fixed boundary conditions. (a) Probability distribution of the transition point $C_c$ from $10^4$ runs with $\bar{A}_{syst} = 10^5$. Solid vertical line: average $C_c$. Dashed vertical lines: average plus or minus one standard deviation $\Delta C_c$. (b) Mean transition threshold $C_c$ as a function of $\bar{A}_{syst}$. Averages are performed on the same number of realizations as in Fig. 5. (From the points from left to right, standard errors of the mean are $7.743 \times 10^{-5}$, $1.685 \times 10^{-4}$, $3.944 \times 10^{-4}$, $3.151 \times 10^{-4}$, $9.1 \times 10^{-4}$) (c) Transition width $\Delta C_c$ (standard deviation) as a function of $\bar{A}_{syst}$. Inset: skewness of transition distributions. Error bars correspond to plus or minus one standard error of the skewness.

### B. Order parameter

Another way to represent the distribution of the transition is to plot the average $\langle \Phi(C) \rangle$ over many realizations, as shown in Fig. 5(b). The average fraction $\langle \Phi(C) \rangle$ can be used as an order parameter to characterize percolation transitions. This choice of order parameter is usual in percolation models Refs. [23,41,43], and in bootstrap percolation models where it corresponds to the fraction of sites in the giant connected component on regular lattice [44,45] or complex networks [46,47].

At small $C$, the behavior of $\langle \Phi(C) \rangle$ is independent of the system size $\bar{A}_{syst}$. An expansion for $C \rightarrow 0$ up to second order in $C$ can be obtained when considering only isolated disks and domains composed of two disks. Such an expansion is

described in detail in Appendix B, and leads to

$$\langle \Phi(C) \rangle = 1 - C + C^2 \left( 2 - \frac{16}{3\pi} \right) + O(C^3). \qquad (6)$$

This expansion captures the behavior of $\langle \Phi(C) \rangle$ for small $C$, as seen in Fig. 14 of Appendix B.

For larger values of $C$, the order parameter $\langle \Phi(C) \rangle$ decreases and vanishes due to the transition. This decrease becomes sharper and occurs at smaller values of $C$ when $\bar{A}_{syst}$ increases, as expected from the decrease of $\Delta C_c$ and $C_c$ reported in Fig. 6.

In addition, the difference between the values of $\langle \Phi(C) \rangle$ for periodic and nonperiodic boundary conditions shown in Fig. 5(b) is seen to decrease when the system size increases. This suggests that the type of boundary condition is asymptotically irrelevant for large systems, and that our results for the transition threshold obtained for large nonperiodic systems should also provide an accurate description of large periodic systems.

### C. Cluster size distribution

Let us call $N$ the number of disks in a cluster. The probability distribution $P(N)$ before the transition is reported in Figs. 7(a) and 7(b). For system sizes $\bar{A}_{syst} \in \{10^4, 10^5, 10^6, 10^7, 10^8\}$, we run $\{10^5, 10^4, 10^3, 10^3, 60\}$ realizations of our simulation respectively. Then, we extract the distributions at $C \in \{0.1, 0.2, 0.3, 0.4, C_c = 0.47\}$ for $\bar{A}_{syst} = 10^4$, and at $C \in \{0.1, 0.2, 0.3, C_c\}$ for $\bar{A}_{syst} \in \{10^5, 10^6, 10^7, 10^8\}$, with $C_c \in \{0.423, 0.394, 0.372, 0.355\}$ respectively. We exclude realizations where the system has already undergone a transition (this corresponds to a significant number of runs mainly at $C = C_c$, where roughly half the realizations have transited).

When $C \rightarrow 0$, there are mainly isolated disks and $P(N = 1) \rightarrow 1$, as seen from Fig. 7(d). As shown in Fig. 7(a), fit of $P(N)$ with a stretched exponential ($a_0 \exp[-a_1(N-1)^{a_2}]$) shows that the distribution approaches an exponential distribution when $C \rightarrow 0$, i.e., $a_2 \rightarrow 1$ as $C \rightarrow 0$.

For larger values of $C$, the tails of the distributions for large $N \gg 1$ exhibit a power-law decay $P(N) \sim N^{-\delta}$. The exponent $\delta$, plotted in Fig. 7(b), is independent of $\bar{A}_{syst}$ and varies approximately linearly with $C$:

$$\delta \approx 14.19 - 24.99C. \qquad (7)$$

Such a power-law tail of the distribution would lead to a divergence of the average cluster size if $\delta \rightarrow 2$. Using Eq. (7), this condition suggests a divergence at $C \approx 0.49$. Note that this value is a speculative extrapolation in the sense that it is larger than all the values of $C$ reported in Fig. 7. The mean cluster size $\langle N \rangle$ is reported in Fig. 7(c). As expected, the mean cluster size $\langle N \rangle \rightarrow 1$ as $C \rightarrow 0$. However, the values of $C$ for which the transition can be measured do not allow one to probe the possible divergence of $\langle N \rangle$ at larger $C$.

### D. Domain area distribution

In systems such as those discussed in the Introduction, the initial disks might not be observable, so that the cluster size $N$ might not be a relevant observable quantity. Instead, the
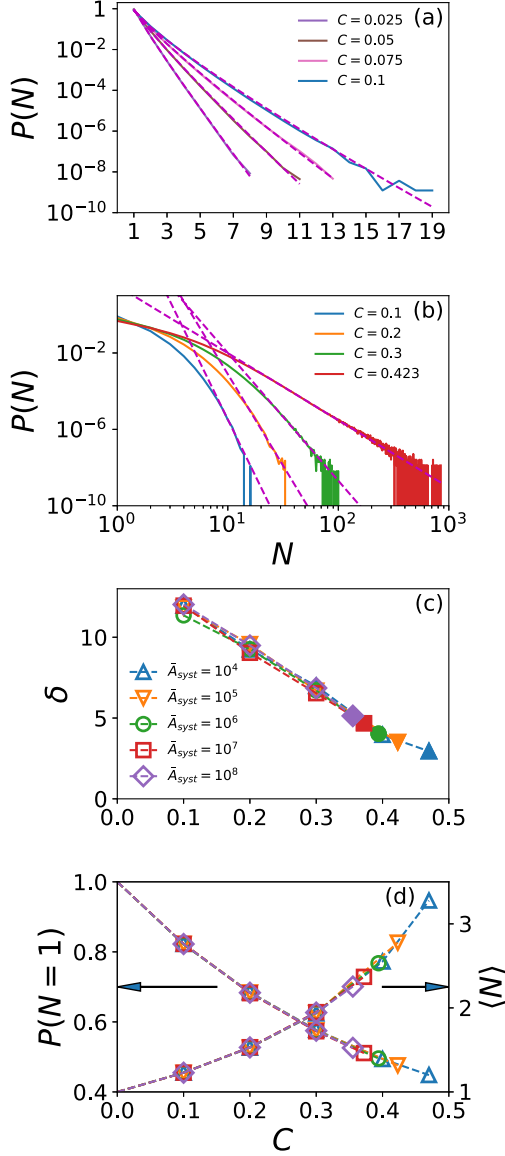
FIG. 8. Cluster area distribution $P(\bar{A})$, for $\bar{A}_{\text{syst}} = 10^5$, averaged over $10^4$ realizations, and $10^5$ realizations for the three curves on the left (small values of $C$); free boundary conditions. From left to right $C = [0.025, 0.05, 0.075, 0.1, 0.2, 0.3, 0.423]$ (the last value of $C$ corresponds to the mean transition point $C_c$). The special values $\bar{A}_{m1}$, $\bar{A}_{m2}$, and $\bar{A}_{m3}$ respectively correspond to the maximal area of a cluster of one, two, and three disks, as discussed in the text.

where $A$ is the domain area.

The domain area probability distribution $P(\bar{A})$, shown in Fig. 8, is found to oscillate at small $\bar{A}$. We observe several oscillations accompanied with discontinuities. First, a Dirac-delta-like peak corresponding to the contribution of domains composed of a single disk at $\bar{A} = \bar{A}_{m1} = 1$. Then, clusters with two disks only have a finite range of domain area $\bar{A}_{m1} < \bar{A} < \bar{A}_{m2}$, and the distribution presents a steplike discontinuity at $\bar{A} = \bar{A}_{m2}$. Possible areas of domains with three disks also obey an inequality $\bar{A}_{m1} < \bar{A} < \bar{A}_{m3}$. This leads to a slope-discontinuity in the area probability distribution at $\bar{A} = \bar{A}_{m3}$. In addition, we observe numerically that there is an approximately horizontal tangent on the right side at $\bar{A} = \bar{A}_{m3}$.

The values of $\bar{A}_{mN}$ for small $N$ correspond to the maximum domain area for a cluster of $N$ disks. For two disks, the configuration with the largest area is obtained for two tangent disks, leading to $\bar{A}_{m2} = 1 + 4/\pi$. For three disks, the configuration with the largest area is obtained when two disks are tangent to the third disk, and when the angle between the two tangent disks is $2\pi/3$, leading to $\bar{A}_{m3} = 1 + (4 + 3^{3/2})/\pi$. As shown in Fig. 8, these values are in agreement with the observed singularities of $P(\bar{A})$. The general question of the existence of higher order $\bar{A}_{mN}$ and the nature of the associated series of singularities remains open.

In contrast to $P(N)$, the tails of $P(\bar{A})$ for large $\bar{A}$ do not obey a clear power law. This is rooted in the nonlinear relation between $A$ and $N$ which is discussed in Appendix F 4. Such a nonlinearity can be interpreted as a finite-size effect for clusters that are not large enough to obey the average-density relation $N \approx \bar{A}C$.

### E. Domain shape

The shape of the domains can be explored via their deviation from circularity. In Fig. 9, we see that the average domain area $A$ for a given perimeter $P$ is proportional to the square of the domain perimeter $P^2$ for large domains. For a circular domain, one has $4\pi A/P^2 = 1$. For large domains, the prefactor is constant and independent of $C$, and one finds $4\pi A/P^2 \approx 0.827$. This constant deviation from circularity for



FIG. 7. Cluster size distribution before transition. (a) $P(N)$ as a function of the number of disks $N$ in the cluster. Small values of $C$: from left to right $C = [0.025, 0.05, 0.075, 0.1]$. System size: $\bar{A}_{\text{syst}} = 10^5$, averaged over $10^5$ realizations. Dashed lines: fits with stretched exponentials $a_0 \exp[-a_1(N-1)^{a_2}]$ with $a_2 = [0.935, 0.909, 0.895, 0.858]$. (b) $P(N)$ for larger values of $C$. Same system size, averaged over $10^4$ realizations (the average is performed over realizations who did not experience a transition). From left to right $C = [0.1, 0.2, 0.3, 0.423]$. Dashed lines: power-law fits of the tails of distribution. (c) Exponent $\delta$ of the tail of the distribution $P(N) \sim N^{-\delta}$ as a function of $C$ for various system sizes $\bar{A}_{\text{syst}}$. (d) Probability of clusters with a single disk $P(N = 1)$, and average cluster size $\langle N \rangle$ as a function of $C$ for various system sizes $\bar{A}_{\text{syst}}$. The symbols refer to the system size $\bar{A}_{\text{syst}}$ and are the same as in (c). Boundary conditions are fixed.

domain area could be observable. As a reminder, a domain is the convex hull of all the disks contained in a cluster. The normalized area of a domain is defined as

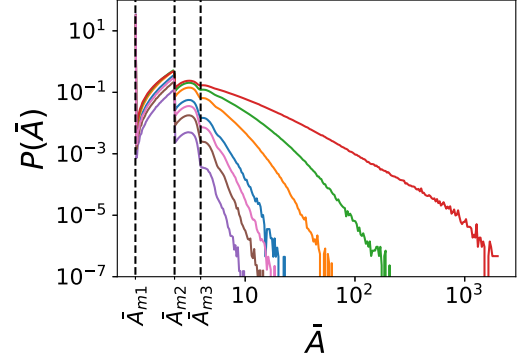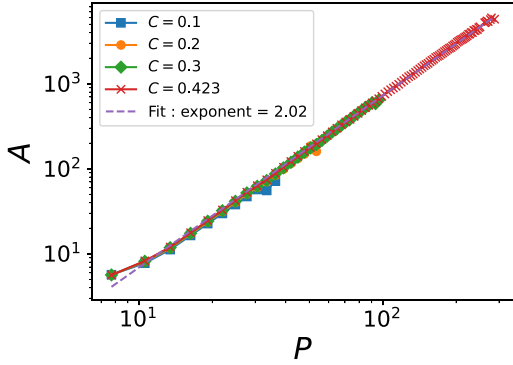$$\bar{A} = \frac{A}{\pi r_d^2}, \qquad (8)$$

FIG. 9. Average cluster area $A$ as a function of the perimeter $P$; same parameters as in Fig. 8.

a wide range of sizes suggests some scale-invariant properties of cluster shapes. Such scale invariance can be associated with the presence of power-law tails of the cluster size distribution discussed in Sec. III C.

## IV. DISCUSSION OF THE TRANSITION

### A. On-lattice bootstrap percolation

As discussed in the Introduction, our model shares strong similarities with bootstrap percolation models. The bootstrap percolation model can be defined as follows. Start with a lattice containing $N_{\text{latt}}$ cells. Initially, $N_a$ cells are activated. Then, each inactive cell is made active if $m$ or more of its nearest neighbors are active. This activation process is performed iteratively up to a final state where no new active cell can be added. Final states corresponding to different values of $N_a$ are plotted in the top panels of Fig. 10 for a periodic square lattice with $m = 2$ and $N_{\text{latt}} = 25^2$. The results look similar to
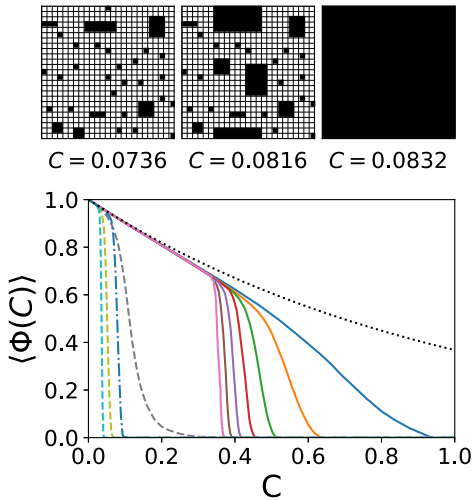


FIG. 10. Comparison with bootstrap percolation. Upper panel: final state of bootstrap percolation model on a square lattice for three different values of the initial concentration $C$. Lower panel: order parameter $\langle \Phi(C) \rangle$ of our model (full lines) and for bootstrap percolation. Dashed lines: square lattice; from right to left, $[10 \times 10; 10^2 \times 10^2; 10^3 \times 10^3]$ cells. Dash-dotted line: hexagonal lattice, $10^2 \times 10^2$ cells.

those of our model, and the system is invaded completely for large-enough $N_a$.

To compare bootstrap percolation with our results, we need to define $C$ in bootstrap percolation. Our procedure for the initial activation of the cells is designed to parallel the continuum case. We choose a site randomly $N_i$ times. Sites can be chosen more than once. If the chosen site is not active, we activate it. In Eq. (2), the normalized concentration $C$ was defined as the total area of all the disks deposited in the system, $N_d \pi r_d^2$, divided by the system area $A_{\text{syst}}$. By analogy, we define the normalized concentration $C$ for on-lattice bootstrap percolation as the total number of times $N_i$ that a site is chosen divided by the total number of sites in the system $N_{\text{latt}}$:

$$C = \frac{N_i}{N_{\text{latt}}}. \tag{9}$$

Indeed, if we associate with each site the area $a_{\text{latt}}$ of the unit cell of the lattice, this definition can be seen as a ratio of the total deposited area $N_i a_{\text{latt}}$ over the total system area $N_{\text{latt}} a_{\text{latt}}$ as in Eq. (2).

The probability of sites not being activated initially is $(1 - 1/N_{\text{latt}})^{N_i} \approx e^{-N_i/N_{\text{latt}}}$ for $N_{\text{latt}} \gg 1$, and the average initial fraction of nonactive sites is therefore

$$\Phi_b(C) = e^{-C}, \tag{10}$$

which is identical to Eq. (3). The average number of initially active cells is then $N_a = N_{\text{latt}}[1 - \Phi_b(C)]$.

A comparison of the numerical results of our model with those of bootstrap percolation is reported in the lower panel of Fig. 10.

Note that curves showing $\langle \Phi \rangle$ for bootstrap percolation are well known, but they are usually plotted as a function of $N_a/N_{\text{latt}} = 1 - \Phi_b$; see, e.g., Refs. [44–47]. The behavior of the two models is similar, as expected. Both models give rise to a transition when $C$ is increased. However, the transition occurs at much smaller values of $C$ for bootstrap percolation.

In order to gain further insight, we have also implemented bootstrap percolation on a hexagonal lattice [4], with $m = 3$ instead of $m = 2$ for the square lattice (indeed, one cell has six nearest neighbors on a hexagonal lattice, instead of four on a square lattice). Due to their six-old symmetry, hexagonal lattices can naively be considered as more isotropic than square lattices. As seen in Fig. 10, the bootstrap transition for a hexagonal lattice is shifted to larger values of $C$ as compared to that of a square lattice, although the transition is still expected to occur at $C \to 0$ in large systems [5]. We speculate that this could be an indication that isotropy shifts the transition to larger $C$ for finite system sizes. This trend would be consistent with the observation of transitions at larger $C$ in our isotropic continuum model.

The bootstrap percolation transition on a square lattice is known to obey [6,48,49]

$$\lim_{\substack{\Phi_b \to 1 \\ A_{\text{syst}} \to \infty}} (1 - \Phi_b) \ln \bar{A}_{\text{syst}} = \frac{\pi^2}{9}. \tag{11}$$

Assuming that the convexification model can be viewed as a continuous and isotropic limit of bootstrap percolation, a naive analogy based on the assumption that the microscopic properties of the models are irrelevant at large scales would

suggest that $C_c \sim (\ln \bar{A}_{\text{syst}})^{-1} \to 0$ as $\bar{A}_{\text{syst}} \to \infty$ in the convexification model.

### B. Transition in the limit of small $C$ and large $\bar{A}_{\text{syst}}$

Our numerical results reported for the convexification model in Sec. III A are obtained in systems that are too small to investigate a possible scaling regime similar to Eq. (11). However, we can simply parallel the heuristic derivation of the asymptotic behavior as discussed in Refs. [48,49]. The details of this analysis are reported in Appendix C. The results are similar to those of usual on-lattice bootstrap percolation and suggest that $C_c \sim (\ln \bar{A}_{\text{syst}})^{-2/3} \to 0$ as $\bar{A}_{\text{syst}} \to \infty$.

The only difference with on-lattice bootstrap percolation is the exponent 2/3. This difference comes from the fact that the increase of cluster area $A$ due to merging with one active site is proportional to the length of a facet of the cluster edge $\sim A^{1/2}$ in on-lattice bootstrap percolation, while it is $\sim A^{1/4}$ for the merging of a cluster with a single disk in the convexification model, as discussed in Appendix C. However, our simulations are too small to assess the validity of this exponent, or to determine the range of values of $C$ for which this exponent would be expected. Further investigations would therefore be needed to clarify the scaling behavior as $\bar{A}_{\text{syst}} \to \infty$.

### C. Transition at finite $C$

Experimental systems usually exhibit a finite size, and it is therefore important to study the behavior of the transition for finite $C$. Inspired by the heuristic derivation of Refs. [48,49], we propose again a heuristic analysis to probe the transition in the regime $C \gtrsim 0.1$. One difficulty in the analysis of the finite concentration regime comes from the relevance of clusters of all sizes, while we could assume that the system was mainly composed of isolated disks in the limit $C \to 0$.

Following Refs. [48,49], our analysis is based on the assumption that the largest cluster is the one that invades the system. The statistics of the largest cluster is studied in Appendix E. We account for the presence of power-law tails of $P(N)$ reported in Sec. III C, and the predictions are in good agreement with the simulations.

The analysis reported in detail in Appendix F is based on a scenario in two steps. First, the largest cluster starts to grow, and then this growth produces a macroscopic avalanche which spans the whole system. The results suggest that, as in on-lattice bootstrap percolation, the transition is governed by the propagation of a macroscopic avalanche.

This analysis reproduces qualitatively the decrease of the transition threshold with $C$, but predicts a threshold which is quantitatively lower. Moreover, no true scaling regime emerges in this regime. We attribute this absence of scaling to the absence of a linear relation between the number $N$ of disks in a domain and the domain area $\bar{A}_N$ in clusters of finite size. However, it is possible to fit the decrease of the threshold using a power law, and we find that $C_c \sim \bar{A}_{\text{syst}}^{-\alpha_c}$ with $\alpha_c \approx 0.032$. Using a fit of the simulation results in the range $10^6 \leqslant \bar{A}_{\text{syst}} \leqslant 10^8$, we obtain a similar but smaller exponent $\alpha_c \approx 0.024$.
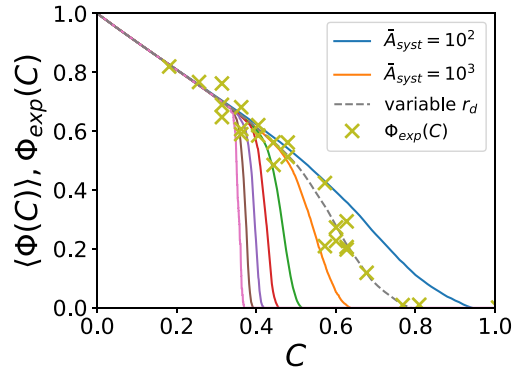


FIG. 11. Comparison of the convexification model with experimental de-adhesion data. Full lines: simulations where $C$ is varied by adding disks one by one. Dashed lines: simulations with variable $r_d$. Crosses: experimental data of [23].

To summarize this section, our simple model inspired by Refs. [48,49] captures the qualitative behavior of the transition, but is unable to reach quantitative agreement.

## V. COMPARISON WITH EXPERIMENTAL RESULTS ON GRAPHENE DE-ADHESION

### A. Model for graphene de-adhesion

In this section, we compare our results with the experimental data from [23] on the de-adhesion of graphene caused by the intercalation of nanoparticles. Following [23], the radius of the detachment zone around a single isolated nanoparticle with diameter $d$ can be approximated by the radius of detachment associated with a vertical point force lifting the membrane up to a distance $d$ from the substrate. Solving the Föppl-von Kármán equations [23,50,51], one obtains

$$2R = \left(\frac{4nG}{3\gamma}\right)^{\frac{1}{4}} d, \tag{12}$$

where $nG$ is the tensile rigidity of the $n$-layer graphene, and $\gamma$ is the adhesion energy per unit area of graphene on silica. Using the experimental values reported in Ref. [23], $d = 7.4 \pm 2.2$ nm, $G = 2.12 \times 10^3$ eV/nm$^2$, and $\gamma = 1.7 \pm 1.1$ eV/nm$^2$, we find $R \approx 23.6 n^{1/4}$ nm. Moreover, we have $C = \rho \pi R^2$, where $\rho$ is the density of nanoparticles. In the experiments of Ref. [23], $\rho = 160 \pm 24$ μm$^{-2}$. Inserting these values into Eq. (12), we obtain $C = \alpha n^{1/2}$, where $\alpha = 0.28 \pm 0.16$. Note the large uncertainty on $\alpha$, which is dominated by the uncertainty in the particle diameter. A fit of the experimental data for the experimental order parameter $\Phi_{\text{exp}}$ at small $C$ prior to transition where $\Phi(C) \approx 1 - C \approx 1 - \alpha n^{1/2}$ leads to $\alpha \approx 0.18$, which is consistent with the estimate of $\alpha$ reported above.

### B. Variable $r_d$ simulations

An inspection of Fig. 11 suggests that the transition observed for experimental data corresponds to a system size $\bar{A}_{\text{syst}}$ between $10^2$ and $10^3$. However, in experiments, the number $n$ of layers of graphene varies, and therefore from Eq. (12) the radius $r_d$ of individual detachment disks varies while the density $\rho$ of particles remains constant.
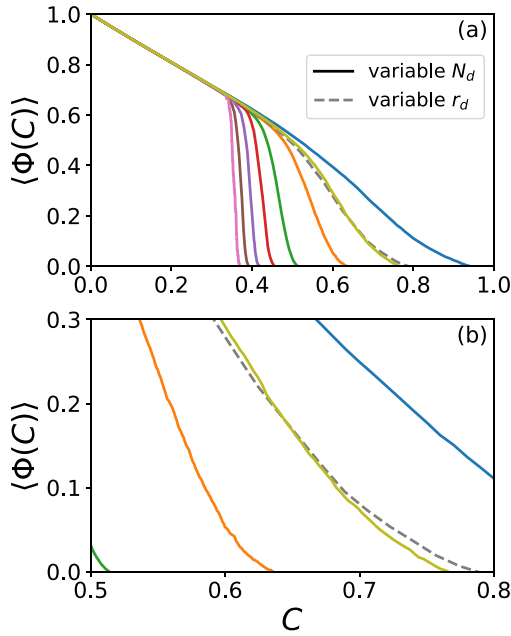
FIG. 12. $\langle \Phi(C) \rangle$ for variable $r_d$; same parameters as in Fig. 5. Full lines: we explore $C$ by adding disks one by one, i.e., by varying $N_d$ for a constant radius of disks $r_d = 1$. Dashed line: we explore $C$ by varying $r_d$, for a fixed number of disks $N_d = 200$ (we keep $A_{\text{syst}} = 200\pi$ fixed and $r_d$ varies from 0 to 1, so that $\bar{A}_{\text{syst}}$ varies from $+\infty$ to 200). To see that the variable $r_d$ curves cross the variable $N_d$ curves, we also show a variable $N_d$ curve for $\bar{A}_{\text{syst}} = 307.7$ (light-green curve).

To model these conditions, we performed simulations where $r_d$ varies while the number of disks $N_d$ and the system area $A_{\text{syst}}$ remain constant. The disk radius $r_d$ is varied from 0 to $r_{d\,\text{max}} = [A_{\text{syst}}/(\pi N_d)]^{1/2}$. Using Eq. (2), this leads to a variation of $C = \pi r_d^2 N_d / A_{\text{syst}} = r_d^2 / r_{d\,\text{max}}^2$ from 0 to 1. In terms of dimensionless numbers, the result of the simulations with variable $r_d$ corresponds to varying $C$ at fixed $N_d$, as opposed to the variable $N_d$ simulations discussed in the previous sections, which correspond to varying $C$ at fixed $\bar{A}_{\text{syst}}$.

To make the link between these two types of simulations, note that increasing $r_d$ corresponds to increasing $C$ and decreasing $\bar{A}_{\text{syst}}$ simultaneously. Hence, increasing $r_d$ can be seen as continuously switching to lower and lower values of $\bar{A}_{\text{syst}}$ when increasing $C$. However, we observe in Fig. 12 that the curve $\langle \Phi(C) \rangle$ as a function of $C$ for a given value of $\bar{A}_{\text{syst}}$ is always below the $\langle \Phi(C) \rangle$ curve for a lower value of $\bar{A}_{\text{syst}}$. Hence, the variable $r_d$ procedure leads to smaller slopes for the decrease of $\langle \Phi(C) \rangle$ as a function of $C$. Indeed, we see that the variable $r_d$ curves have a smaller slope and cross the variable $N_d$ curves in Fig. 12. As a consequence, the width of the transition along $C$ is slightly larger with the variable $r_d$ procedure.

### C. Results

As shown in Fig. 11, agreement with experiments is found for $N_d \approx 2 \times 10^2$. Our results therefore suggest a finite-size effect involving about $N_d = 200$ particles in experiments. Translating $N_d$ into a length scale defined as the diameter of a circular zone including 200 disks, we find $2(N_d/\pi \rho)^{1/2} \approx$

1.3 μm. However, the physical mechanism at the origin of this length scale is not known. For example, correlations between nanoparticle positions, or elastic effects, could come into play.

## VI. CONCLUSION

In conclusion, we have introduced a model for invasion in two dimensions based on the convexification and merging of domains. Starting with an initial condition where disks of equal diameter are randomly placed in the plane, we find an invasion transition. An analogy with on-lattice bootstrap percolation suggests that the invasion threshold should be observed at zero density when the system size tends to infinity. Our numerical simulations do not allow us to investigate the asymptotic behavior for very small disk densities. We hope that our work will motivate further studies of the convexification model. Indeed, theoretical investigations and large-scale numerical simulations are needed to elucidate the low-density and large scale asymptotic properties of the model. It would also be interesting to investigate on-lattice bootstrap percolation to determine if power-law tails are also present for these models in the finite $C$ regime.

In the regime of finite densities $C \gtrsim 0.1$, which should be the relevant one for most experimental systems, we found that the cluster-size distribution has a power-law tail, with an exponent that increases linearly with the disk density. In this regime, the deviation from circularity of the average shape of large clusters is constant.

Furthermore, in both finite and small concentration regimes, we found that the domain area distribution oscillates for small areas. These oscillation are accompanied by singularities of the distribution.

Our results compare favorably with experimental data on the unbinding transition of graphene with intercalated nanoparticles reported in Ref. [23]. Other experimental applications of the model would be welcome to strengthen the claim of genericity and universality of domain invasion via convexification. Indeed, our results could also describe invasion transitions in line-tension induced growth of two-dimensional domains with random impurities or defects, including magnetic domains, adsorption of a monolayer of molecules or particles with short-range attractive interactions on a substrate, and imbibition in Hele-Shaw geometry. As discussed in the Introduction, our model could also pertain to population dynamics, classification and clustering of points or domains in the plane, and separation of objects in images.

## APPENDIX A: CONVEX HULLS WITH PERIODIC BOUNDARY CONDITIONS

In the periodic case, the algorithm is similar to that described above. However, a novel situation appears when a
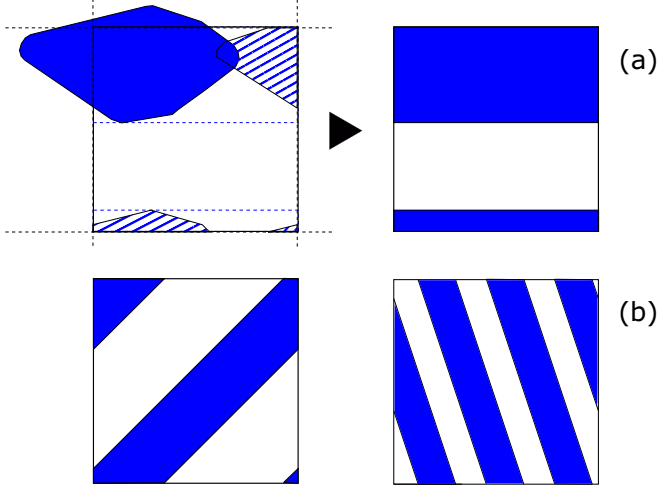
FIG. 13. (a) The convex hull of a cluster overlapping with its image through the periodic boundary conditions is a striplike domain. (b) The strip may wrap around the system an arbitrary number of times in both directions.

domain is in contact with its periodic image, as shown in Fig. 13(a). The domain is then made convex only along the direction where it is in contact with its periodic image, leading to a striplike convex hull. To include all possible cases, since our square periodic simulation box has a toruslike topology, we have to consider situations where the domain wraps around the boundary conditions several times, as shown on Fig. 13(b).

Strips are convex domains in the sense that, given two points belonging to the strip, it is possible to find a segment that connects these two points with all points of the segment also belonging to the strip. However, in contrast to usual convex shapes in the plane, for a given strip it is possible to find a segment connecting two points of the strip with a part of the segment not belonging to the strip. More precisely, strips appear when defining a convex domain as a domain that contains all the straight segments between two points of the domain if these two points can be merged to one point by a continuous transformation that keeps them inside the domain. Equivalently, strips can be defined by moving to the full infinite plane, tiled by our square system and all its periodic images and taking the convex hull of each connected components.

Periodic systems have the advantage of not having boundaries that could make them spatially inhomogeneous as in the case of fixed boundary conditions. However, the periodicity itself imposes discrete global symmetries that make the strips anisotropic. These symmetries here are those of the square tiling of the plane, and the related anisotropy is expressed in the fact that the orientation of the strips cannot take arbitrary values and are limited to rational slopes in the $x, y$ plane.

In addition, when the domain is in contact with its periodic image in two orthogonal directions, the convex hull is the whole simulation box. In practice for large system size, each time the addition of a disk provoked the appearance of a strip, the process of iterative convexification continued and led to the full invasion of the domain by this strip.

## APPENDIX B: LOW-$C$ EXPANSION FOR $\langle \Phi(C) \rangle$

In the following, we report on two expansions of $\langle \Phi(C) \rangle$ in the limit $C \to 0$.

### 1. Expansion from area occupied by the sum of all disk areas

The first strategy is to use the situation where each disk contributes to decreasing the free area by their own area $\pi r_d^2$ as a leading order estimate. This leads to a first estimate of the fraction of the system area that is not covered by the domains:

$$\langle \Phi(C) \rangle_{a0} = 1 - C. \tag{B1}$$

In the limit of low density $C \to 0$, this expression is valid to linear order in $C$ because the density of disks is very low so that the probability that disks overlap vanishes.

A first correction to this approximation is to consider the effect of dimers, i.e., clusters made of two overlapping disks. Overlapping occurs if another disk is present at a distance smaller than $2r_d$. For each dimer, the area not covered by the domains must be corrected by an amount

$$\Delta A = \pi r_d^2 - 2r r_d, \tag{B2}$$

where $r$ is the distance between the centers of the two disks. Hence, in the presence of a concentration $\rho_d$ of disks, the correction is

$$\langle \Phi(C) \rangle_{a1} = \frac{1}{2} \rho_d \int_0^{2r_d} dr \, 2\pi r \rho_d \Delta A = C^2 \left( 2 - \frac{16}{3\pi} \right). \tag{B3}$$

where the $1/2$ prefactor accounts for the fact that each dimer is counted two times (one time starting from the first disk, and another time starting from the second disk). The correction $\langle \Phi(C) \rangle_{a1}$ is positive: on average over all distances $r$, the positive contribution coming from the overlapping area of the disks is larger than the negative contribution due to the convexification.

### 2. Expansion from the empty area

Another strategy is to perform an expansion from the area that is empty in the presence of the overlapping disks before any convexification is performed. We then start with

$$\langle \Phi(C) \rangle_{e0} = \Phi_p(C) = e^{-C}, \tag{B4}$$

which is consistent with Eq. (B1) to linear order in $C$.

A dimer correction is then obtained considering a different area change that has to account for the fact that overlapping of disks is already present in the reference state,

$$\Delta A = r_d^2 \left[ \pi - 2u + u \left( 1 - \frac{u^2}{4} \right)^{1/2} - 2 \arccos \frac{u}{2} \right], \tag{B5}$$

where $u = r/r_d$. We then obtain

$$\langle \Phi(C) \rangle_{e1} = \frac{1}{2} \rho_d \int_0^{2r_d} dr \, 2\pi r \rho_d \Delta A = C^2 \left( \frac{3}{2} - \frac{16}{3\pi} \right). \tag{B6}$$
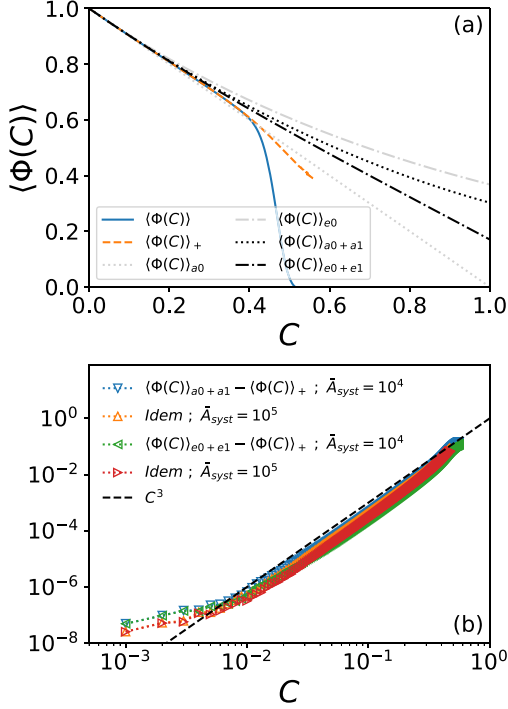
FIG. 14. Low-$C$ expansion of the order parameter $\langle \Phi(C) \rangle$. (a) Comparison with simulations for $\bar{A}_{syst} = 10^4$. Solid line: $\langle \Phi(C) \rangle$ from simulations. Dashed line: average of $\Phi(C)$ in systems that have not undergone a transition $\langle \Phi(C) \rangle_+$. Dotted lines: first expansion $\langle \Phi(C) \rangle_{a0}$ and $\langle \Phi(C) \rangle_{a0+a1} = \langle \Phi(C) \rangle_{a0} + \langle \Phi(C) \rangle_{a1}$. Dashed-dotted lines: second expansion $\langle \Phi(C) \rangle_{e0}$ and $\langle \Phi(C) \rangle_{e0+e1} = \langle \Phi(C) \rangle_{e0} + \langle \Phi(C) \rangle_{e1}$. The leading order expressions are shown in lighter tone (gray). (b) Deviation of simulation results from low-$C$ predictions.

In contrast to Eq. (B3), the correction $\langle \Phi(C) \rangle_{e1}$ is now negative because it only results from the negative contribution of convexification.

The Taylor expansion of the two approximations is identical up to second order in $C$, i.e.,

$$\langle \Phi(C) \rangle = \langle \Phi(C) \rangle_{a0} + \langle \Phi(C) \rangle_{a1} + O(C^3)$$
$$= \langle \Phi(C) \rangle_{e0} + \langle \Phi(C) \rangle_{e1} + O(C^3)$$
$$= 1 - C + C^2 \left( 2 - \frac{16}{3\pi} \right) + O(C^3). \quad (B7)$$

### 3. Comparison of the low-$C$ expansions with numerical results

As seen in Fig. 14(a), low-$C$ expansions of $\langle \Phi(C) \rangle$ are in good agreement with numerical simulations at small $C$. Numerical results for the average $\langle \Phi(C) \rangle_+$ in systems that have not undergone a transition is also reported. This latter quantity deviates from $\langle \Phi(C) \rangle$ in the transition region.

The deviation from the expansions, reported in Fig. 14(b), scales as $C^3$ as expected from Eq. (B7). Some deviations are observed for $C$ smaller than $10^{-2}$. These deviations are caused by the finite size of the system that does not present enough dimers at small $C$ for the expansions to be valid.

## APPENDIX C: ANALOGY WITH HEURISTIC DISCUSSION OF ON-LATTICE BOOTSTRAP PERCOLATION AT SMALL $C$

In this section, we apply the heuristic derivation of the asymptotic behavior of the transition for on-lattice bootstrap percolation [48,49] to the case of our convexification model.

Consider a large domain. In the limit $C \to 0$, there are very few large clusters, and we therefore analyze the growth of a cluster by merging with isolated disks. The probability $P^-(A)$ of not growing for a domain of perimeter $A$ is the probability of having no disk in a region of width $r_d$ around the periphery of the domain. Denoting the area of this region as $A_e$, we have

$$P^-(A) = e^{-A_e \rho_d}. \quad (C1)$$

In normalized variables $\bar{A}_e = A_e / (\pi r_d^2)$,

$$P^-(\bar{A}) = e^{-\bar{A}_e C}. \quad (C2)$$

Hence, in the limit $C \to 0$, the probability of growing is

$$P^+(\bar{A}) = 1 - e^{-\bar{A}_e C} \approx \bar{A}_e C. \quad (C3)$$

Assuming that the cluster is large and circular of radius $R$, we have

$$\bar{A}_e = \frac{A_e}{\pi r_d^2} = \frac{2\pi R r_d}{\pi r_d^2} = 2 \frac{(A/\pi)^{1/2}}{r_d} = 2 \bar{A}^{1/2}. \quad (C4)$$

Growth of the largest cluster of area $\bar{A}_c$ at the critical concentration $C_c$ requires $P^+(\bar{A}_c) = a$, where $a$ is a constant, leading to the condition

$$2 \bar{A}_c^{1/2} C_c \approx a. \quad (C5)$$

Let us now investigate the growth of the cluster via mergings with disks. Consider first the merging of a cluster with one disk. Assuming that clusters are circular with radius $R$, the increase of the cluster area due to merging is

$$\Delta A = (R^2 - r_d^2)(\tan \theta - \theta), \quad (C6)$$

where $\cos \theta = (R - r_d)/d$, with $d$ the distance between the center of the cluster of radius $R$ and the disk. In the limit of interest where $R \gg r_d$, we have

$$\Delta A = \frac{2^{3/2}}{3} R^{1/2} (1 + \alpha)^{3/2} r_d^{3/2}, \quad (C7)$$

where $\alpha = (d - R)/r_d$ obeys $-1 \leqslant \alpha \leqslant 1$. Assuming a uniform distribution of $\alpha$ in the interval $[-1, 1]$, we approximate the term $(1 + \alpha)^{3/2}$ by its the average value,

$$(1 + \alpha)^{3/2} \approx \frac{1}{2} \int_{-1}^{1} d\alpha (1 + \alpha)^{3/2} = \frac{2^{5/2}}{5}. \quad (C8)$$

The normalized area of the cluster after the $n$th mergings obeys

$$\bar{A}_n = \bar{A}_{n+1} + \Delta \bar{A}_n. \quad (C9)$$

From Eqs. (C7) and (C8), and assuming that all clusters are circular, we have

$$\Delta \bar{A}_n = \frac{2^4}{15\pi} \bar{A}_n^{1/4}. \quad (C10)$$

Taking the continuum limit in $n$, and integrating over $n$, we obtain

$$\bar{A}_n = \left\{ \frac{2^2}{5\pi}(n + n_0) \right\}^{4/3}, \tag{C11}$$

where $n_0$ is a constant that will be neglected in the limit of large $n$.

The probability of having a cluster of size $\bar{A}_n$ obeys the recursion relation

$$P(\bar{A}_{n+1}) = P^+(\bar{A}_n)P(\bar{A}_n). \tag{C12}$$

Combining this relation with Eq. (C3) leads to

$$P(\bar{A}_{n+1}) = 2\bar{A}_n^{1/2}CP(\bar{A}_n). \tag{C13}$$

Hence, using Eq. (C11), we have

$$P(\bar{A}_n) = P(1) \prod_{m=1}^{n-1} 2C \left\{ \frac{2^2}{5\pi}m \right\}^{2/3}. \tag{C14}$$

Assuming that $P(1) \approx C$, we obtain

$$P(\bar{A}_n) = C^n [(n-1)!]^{2/3} \left\{ \frac{2^{7/3}}{(5\pi)^{2/3}} \right\}^{n-1}. \tag{C15}$$

We then impose the condition that there is a cluster of size $\bar{A}_{n_c}$ with a finite probability $b$ at the threshold

$$\bar{A}_{\mathrm{syst}}P(\bar{A}_c) = b. \tag{C16}$$

Using the Stirling formula and Eq. (C11), this condition leads to

$$C_c[2\pi(n_c - 1)]^{1/3} \left\{ \frac{2}{e^{2/3}}C_c\bar{A}_c^{1/2}\left(1 - \frac{1}{n_c}\right)^{2/3} \right\}^{n_c - 1} = \frac{b}{\bar{A}_{\mathrm{syst}}}. \tag{C17}$$

Using Eq. (C5), and assuming again $n_c \gg 1$, we obtain

$$C_c(2\pi n_c)^{1/3} \left\{ \frac{a}{e^{2/3}} \right\}^{n_c} = \frac{b}{\bar{A}_{\mathrm{syst}}}. \tag{C18}$$

Hence to leading order

$$n_c \approx \frac{\ln \bar{A}_{\mathrm{syst}}}{\ln[e^{2/3}/a]}. \tag{C19}$$

Using again Eqs. (C5) and (C11), this relation is rewritten as

$$C_c \approx \frac{a}{2} \left( \frac{2^2}{5\pi} \frac{\ln[e^{2/3}/a]}{\ln \bar{A}_{\mathrm{syst}}} \right)^{2/3}. \tag{C20}$$

Hence, we conclude that $C_c \sim (\ln \bar{A}_{\mathrm{syst}})^{-2/3} \to 0$ as $\bar{A}_{\mathrm{syst}} \to 0$.

## APPENDIX D: LINK BETWEEN CLUSTER NUMBER AND DISK DENSITY

In this Appendix, we derive some relations concerning the average number of clusters, and we define some quantities that will be used in the subsequent appendices.

The total number of disks $N_d$ obeys

$$\sum_{N=1}^{\infty} NM_N = N_d, \tag{D1}$$

where $M_N$ is the average number of clusters of size $N$. Since $P(N) = M_N/M_{\mathrm{cl}}$, where $M_{\mathrm{cl}}$ is the total number of clusters, we have

$$M_{\mathrm{cl}} = \frac{N_d}{\sum_{N=1}^{\infty} NP(N)}. \tag{D2}$$

Defining the moments

$$\mu_k = \sum_{N=1}^{\infty} N^k P(N), \tag{D3}$$

we rewrite Eq. (D2) as

$$M_{\mathrm{cl}} = \frac{N_d}{\mu_1} = \frac{C\bar{A}_{\mathrm{syst}}}{\mu_1}. \tag{D4}$$

## APPENDIX E: LARGEST CLUSTER SIZE IN THE FINITE $C$ REGIME

In this Appendix, we propose an expression for the largest cluster size $N_{\max}$. The analysis is based on the numerical observation of a power-law behavior for the cluster size distribution $P(N) \approx BN^{-\delta}$ for large $N$.

The distribution $P(N)$ is approximated with an ansatz of the form

$$P(N) = \frac{B}{(N_0 + N)^{\delta}}. \tag{E1}$$

where $N_0 > -1$ is a constant. The normalization of $P(N)$,

$$\sum_{N=1}^{\infty} P(N) = 1, \tag{E2}$$

imposes a condition that allows one to determine $N_0$:

$$B\,\zeta[\delta, N_0 + 1] = 1, \tag{E3}$$

where $\zeta$ is the Hurwitz zeta function, defined as

$$\zeta(s, a) = \sum_{n=0}^{\infty} \frac{1}{(n + a)^s}.$$

A simple approximation for the average largest cluster size $N_{\max}$ when choosing $M_{\mathrm{cl}}$ clusters from the distribution $P(N)$ is obtained by the condition that only one cluster has a size larger than $N_{\max}$ [2]. Assuming that $N_{\max} \gg 1$, we can use the continuum limit

$$\int_{N_{\max}}^{\infty} dN\,P(N) = \frac{1}{M_{\mathrm{cl}}}. \tag{E4}$$

Using Eq. (D4), we obtain

$$N_{\max} = \left( \frac{C\bar{A}_{\mathrm{syst}}B}{(\delta - 1)\mu_1} \right)^{1/(\delta - 1)} - N_0, \tag{E5}$$

where

$$\mu_1 = B\,\zeta[\delta - 1, N_0 + 1] - N_0. \tag{E6}$$

## APPENDIX F: HEURISTIC DISCUSSION OF THE TRANSITION IN THE FINITE $C$ REGIME

In the following, we present a heuristic derivation for the expression for the transition probability.

Upon the addition of a new disk, the probability that a macroscopic avalanche occurs is assumed to be the product of two terms: the probability $P_{\text{start}}$ that the growth of the cluster of largest size $N_{\text{max}}$ can be triggered, and the probability $P_{\text{av}}$ that this initial growing cluster gives rise to a macroscopic avalanche that spans the whole system. The probability $Q_{\text{trans}}(N_d)$ that no transition has occurred before $N_d$ therefore obeys

$$Q_{\text{trans}}(N_d + 1) = Q_{\text{trans}}(N_d)(1 - P_{\text{start}}P_{\text{av}}). \quad \text{(F1)}$$

In the following, we obtain expressions for $P_{\text{start}}$ and $P_{\text{av}}$, neglecting corrections due to the system boundary.

### 1. Probability of triggering an avalanche from the merging of a disk with a cluster

In the following, we derive an expression for $P_{\text{start}}$ based on the assumption that growing domain of size $\sim N_{\text{max}}$ is triggered by the deposition of a disk on the largest domain. The probability $P_{\text{start}}$ is therefore the product of the probability $P_{\text{dep}}$ that a newly deposited disk leads to a modification of the edge of the largest cluster and the probability that subsequent growth of the cluster edge occurs after the adding of the first disk.

The probability $P_{\text{dep}}$ is the probability that a new disk is deposited in a zone of width $2r_d$ along the edge of the largest domain, leading to an initial growth of the domain:

$$P_{\text{dep}} = \frac{4\pi R_{\text{max}} r_d}{A_{\text{syst}}} = \frac{4\bar{R}_{\text{max}}}{\bar{A}_{\text{syst}}}. \quad \text{(F2)}$$

The radius $R_{\text{max}}$ of the largest cluster is defined from the relation

$$\pi R_{\text{max}}^2 = A_{N_{\text{max}}} \quad \text{or} \quad \bar{R}_{\text{max}}^2 = \bar{A}_{N_{\text{max}}}, \quad \text{(F3)}$$

where $N_{\text{max}}$ is given by Eq. (E4).

In the following, we derive an approximate expression for the probability that the initial growth of the cluster due to the deposition of a new disk gives rise to subsequent growth by merging with other clusters.

We first simplify the analysis by assuming that all clusters are circular. The probability that a domain of radius $R$ does not grow further after the initial growth due to a newly added disk at its edge is

$$Q_+(R) = \exp\left[-\sum_{N=1}^{\infty} \rho_N \Delta A_N\right], \quad \text{(F4)}$$

where $\rho_N$ is the number density of clusters of size $N$, and $\Delta A_N$ is the area of the region where the center of a merging cluster of radius $R_N$ can be placed. This zone, which is constrained by the fact that the domains of size $R_N$ initially do not overlap with the domains of radius $R$, is depicted in Fig. 15. While the width of this region in the direction perpendicular to the initial position of the edge does not depend on the radius $R_N$ of the merging domain, the width in the other direction is actually proportional to $R + R_N$. Hence, we have

$$\Delta A_N \approx \frac{R + R_N}{R} \Delta A, \quad \text{(F5)}$$

where $\Delta A$ is the area of the initial growth region due to the merging of the domain of radius $R$ with the deposited disk.
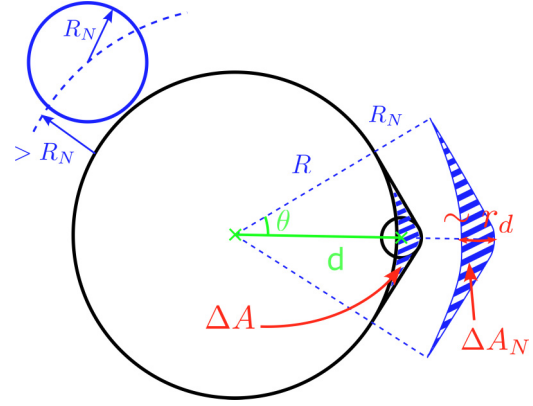


FIG. 15. Schematic for the derivation of the probability that the growth of the cluster due to the deposition of a new disk triggers further merging with other clusters.

Inserting Eq. (F5) in Eq. (F4) and using Eqs. (C7) and (C8), we obtain

$$Q_+(R) = \exp\left[-\frac{2^4}{15} R^{1/2} r_d^{3/2} \sum_{N=1}^{\infty} \rho_N \left(1 + \frac{R_N}{R}\right) \cdot\right] \quad \text{(F6)}$$

Using the relation Eq. (D4), we have

$$\pi r_d^2 \rho_N = \pi r_d^2 \frac{M_N/M_{\text{cl}}}{A_{\text{syst}}/M_{\text{cl}}} = \frac{CP(N)}{\mu_1}. \quad \text{(F7)}$$

We now define

$$\tilde{N} = A_N \rho_d = \bar{A}_N C = \pi R_N^2 \rho_d = \bar{R}_N^2 C. \quad \text{(F8)}$$

where $\bar{R} = R/r_d$. Since the disk density inside clusters is expected to be constant and equal to $\rho_d$ for large clusters, we have $\tilde{N} \to N$ as $N \to \infty$.

Then we obtain

$$Q_+(\bar{R}) = \exp\left[-\frac{2^4}{15\pi\mu_1}\left(\bar{R}^{1/2}C + \frac{C^{1/2}}{\bar{R}^{1/2}}\tilde{\mu}_{1/2}\right)\right] \quad \text{(F9)}$$

with

$$\tilde{\mu}_k = \sum_{N=1}^{\infty} \tilde{N}^k P(N). \quad \text{(F10)}$$

Finally, the probability that the domain of largest size starts to grow, which is approximated by the probability that the first growth gives rise at least to one merging event with another cluster, reads

$$P_{\text{start}} = P_{\text{dep}}[1 - Q_+(\bar{R}_{\text{max}})]. \quad \text{(F11)}$$

### 2. Probability of propagating a macroscopic avalanche

We now derive an expression for $P_{\text{av}}$, the probability that the growth of the domain proceeds indefinitely after the starting regime. The difference between the starting regime and further growth is essentially due to the constraint of nonpenetration of the clusters. In the initial stages of the avalanche, this forbids the presence of clusters of size $N$ at a distance smaller than their radius $R_N$ from the cluster. In the later stages of growth, the edge of the growing domain is not stationary and can be in contact with other clusters. Note, however, that we

neglect the correlations between the clusters other than the growing cluster in all cases.

To evaluate $P_{av}$, we start with the probability of a large growing circular nonstationary domain of radius $R$ not growing, which is the probability that no other domain of size $N$ is in a strip of width $2R_N$ around the edge of the domain. For $R_N \ll R$, the area of the strip is $4\pi R R_N$, and we have

$$Q_{stop}(R) = \exp\left[-\sum_{N=1}^{\infty} \rho_N 4\pi R R_N\right]. \quad (F12)$$

The probability of growing indefinitely is the product of the probability $1 - Q_{stop}(R)$ for all $R$'s that are reached during the growth process. Hence

$$\ln P_{av} = \sum_R \ln[1 - Q_{stop}(R)]$$
$$\approx \int_{R_{max}}^{\infty} \frac{dR}{\Delta R} \ln[1 - Q_{stop}(R)], \quad (F13)$$

where $\Delta R$ is the change of radius due to a merging event. Since we will consider the largest cluster, the other clusters are smaller and one can safely use Eq. (C7) with the substitution $r_d \to R_N$ for the change of area induced by a single merging event. Hence, the change in radius due to one merging is

$$\Delta R = \frac{\Delta A}{2\pi R} = \frac{2^4}{15\pi} \frac{R_N^{3/2}}{R^{1/2}}. \quad (F14)$$

Finally, we obtain

$$P_{av} = \exp\left[\frac{15\pi}{2^7} \frac{\mu_1^{3/2}}{\tilde{\mu}_{3/4}\tilde{\mu}_{1/2}^{3/2}} \int_{x_{max}}^{\infty} dx\, x^{1/2} \ln[1 - e^{-x}]\right], \quad (F15)$$

with

$$x_{max} = \frac{C^{1/2}\tilde{\mu}_{1/2}}{\mu_1} \bar{R}_{max}. \quad (F16)$$

### 3. Transition probability

Changing variable from $N_d$ to $C$ in Eq. (F1), taking the continuum limit, and using the relation $dN_d/dC = \bar{A}_{syst}$, we obtain a differential equation:

$$\frac{d}{dC} Q_{trans}(C) = -4\bar{R}_{max}[1 - Q_+(\bar{R}_{max})]P_{av}Q_{trans}(C), \quad (F17)$$

which is solved with the initial condition $Q_{trans}(0) = 1$ as

$$Q_{trans}(C) = \exp\left[-4\int_0^C dC\, \bar{R}_{max}[1 - Q_+(\bar{R}_{max})]P_{av}\right]. \quad (F18)$$

The numerical evaluation of $Q_{trans}(C)$ for some given system size $\bar{A}_{syst}$ requires the evaluation of the quantities $\mu_1$, $\tilde{\mu}_{1/2}$, and $\tilde{\mu}_{3/4}$ that depend on $C$, and $\bar{R}_{max}$ that depends on $C$ and $\bar{A}_{syst}$.

### 4. Numerical methods

For the numerical evaluation of $Q_{trans}(C)$, we use a strategy based on parametric analytical formulas that fit the numerical results for $\delta(C)$, $B(C)$, and $\bar{A}_N$ in the range of $0.1 \leqslant C \leqslant C_c$ where we have measured $P(N)$ and $A_N$ numerically. These

analytical formulas have no theoretical basis. However, we report in the main text the strikingly simple linear behavior of the exponent $\delta(C)$. As an important remark, the precise form of these formulas should not influence our results since they are essentially used for interpolation. In contrast, the power-law behavior $P(N) \sim N^{-\delta}$ is crucial since it has been used for extrapolation to large $N$ in Eq. (E4) to determine the size of the largest cluster $N_{max}$.

The first step in these evaluations is to determine the dependence of $\delta$ and $B$ on $C$. The variation of $\delta$ with $C$ is given by Eq. (7). In addition, we use

$$B = \frac{b_2}{1 + e^{b_0(C-b_1)}}. \quad (F19)$$

As seen Fig. 16(a) this expression captures the variation of $B$ with $C$ when $b_0 = 60$, $b_1 = 0.25$, and $b_2 = 1.4 \times 10^6$.

Then, using Eqs. (E4), (E6), and (E3), we can directly evaluate $\mu_1$ and $N_{max}$. The expression Eq. (E4) for $N_{max}$ is found to be in good agreement with our numerical results, as seen from Fig. 17(a).

However, the evaluation of $\tilde{N}_{max} = \bar{A}_{N_{max}}$ and $\tilde{\mu}_n$ requires a careful study of the dependence of $A_N$ on $N$. Since the concentration of disks is homogeneous in the plane, we expect asymptotic behavior $\bar{A}_{N\to\infty} \to N/C$. However, as seen in Fig. 16(b), this behavior is observed only for the largest clusters and for $C \geqslant 0.4$. To account for the deviations at small $C$ and $N$, we propose a functional form

$$\bar{A}_N = 1 + \frac{N-1}{C}\left(1 - e^{-a_0(N+a_3)^{a_1}C^{a_2}}\right). \quad (F20)$$

where $a_i$, $i = 0, \ldots, 3$ are constants. This expression presents the expected asymptotic behavior for large $N$, and also imposes the correct behavior for $N = 1$, i.e., $\bar{A}_{N=1} = 1$. Moreover, we see that $\bar{A}_N$ does not diverge for $C \to 0$ when $a_2 \geqslant 1$. The behavior of $\bar{A}_N$ is captured for all values of $C$ with $a_0 = 0.6$, $a_1 = 0.42$, $a_2 = 1.1$, and $a_3 = 1.3$, as seen in Fig. 16(c).

Using Eq. (F20), we can now determine

$$\bar{R}_{max} = \bar{A}_{N_{max}}^{1/2} \quad (F21)$$

and

$$\tilde{\mu}_k = \sum_{N=1}^{\infty} (C\bar{A}_N)^k P(N). \quad (F22)$$

### 5. Results

The evaluation of $Q_{trans}(C)$ leads to a behavior that shares similarities with the full numerical simulations reported in the main text. Indeed, a transition is seen as a sharp drop of $Q_{trans}$ in Fig. 17(b). When the system size $\bar{A}_{syst}$ is increased, average transition value and transition width decrease, as reported in Fig. 6.

A limitation of the analytical model is the breakdown of the analytical description when $C \gtrsim 0.45$, due to the divergence of $\mu_1$ when $\delta \to 2$. This effect is important for small $\bar{A}_{syst}$, when the transition region spreads to large values of $C$. However, this does not affect the transition for large enough $\bar{A}_{syst}$.

The average location of the transition can be inferred from the transition probability density $-dQ_{trans}/dC$, leading to a
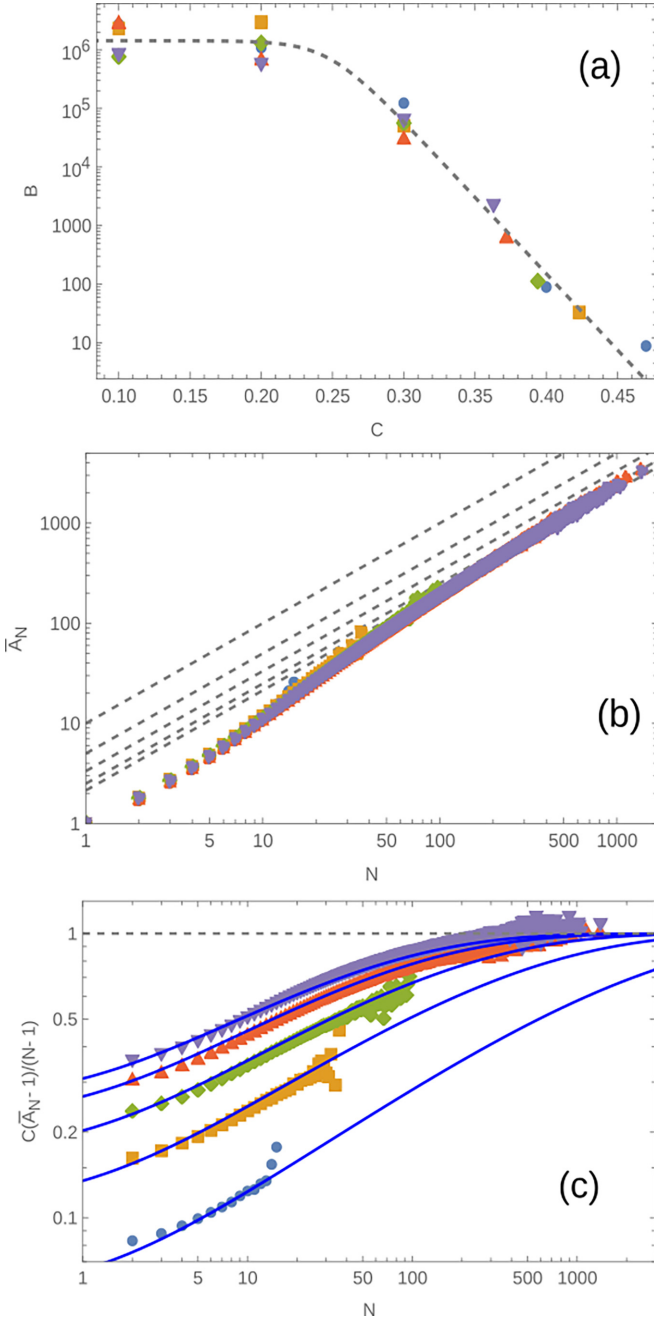
FIG. 16. (a) Parameter $B$ extracted from simulation data as a function of $C$. Circles, squares, diamonds, up-triangles, and down-triangles correspond to system sizes $10^8$, $10^7$, $10^6$, $10^5$, and $10^4$ respectively. (b) Cluster area $A_N$ as a function of the number of disks $N$ for $\bar{A}_{\text{syst}} = 10^5$. Circles, squares, diamonds, up-triangles, and down-triangles correspond to $C = 0.1$, 0.2, 0.3, 0.4, and 0.468. Dashed lines are $\bar{A}_N = N/C$. For concentrations lower than 0.4, the asymptotic behavior $A_N \approx N/C$ is not reached in our simulations. (c) Normalized area distribution $C(\bar{A}_N - 1)/(N - 1)$. Lines are comparison to Eq. (F20).

transition at

$$C_c = -\int_0^{C_{\max} \to \infty} dC\, C \frac{d}{dC} Q_{\text{trans}} = \int_0^{C_{\max} \to \infty} dC\, Q_{\text{trans}}.$$
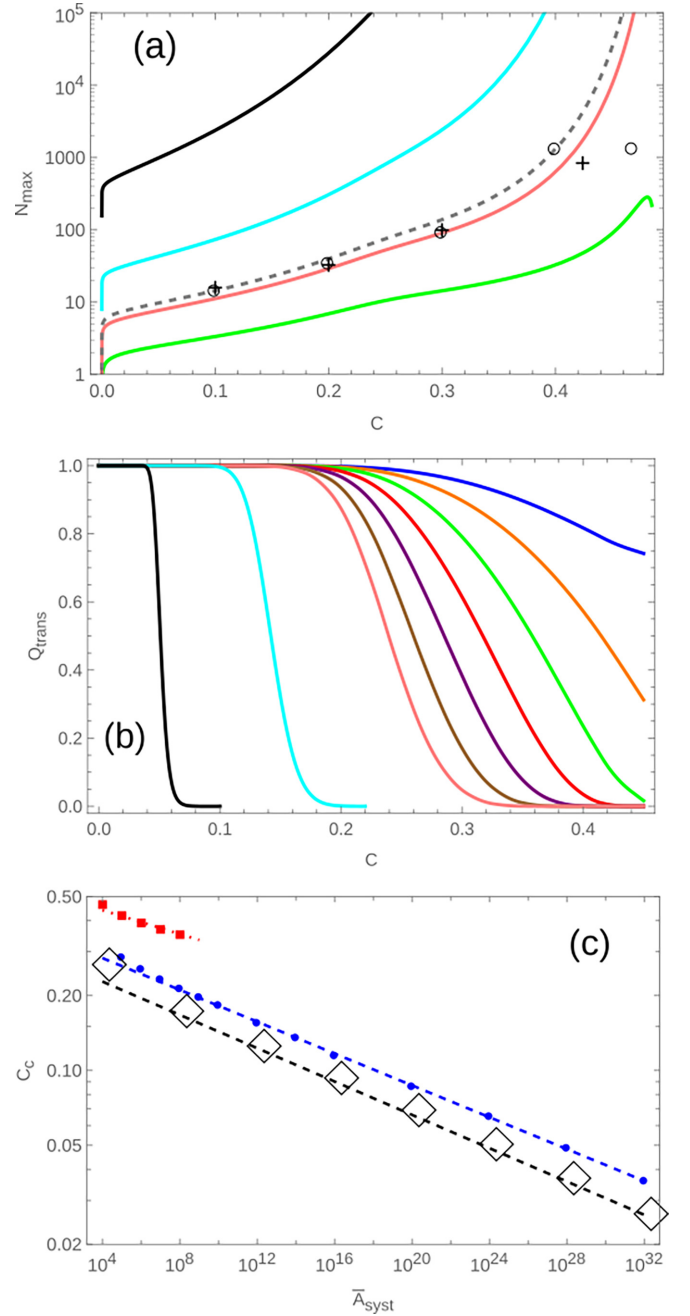
(F23)



FIG. 17. (a) Maximum cluster size. The circles are obtained with the data of Fig. 7, where $10^4$ simulations were performed in a system of size $\bar{A}_{\text{syst}} = 10^5$. The pluses correspond to $10^5$ simulations with $\bar{A}_{\text{syst}} = 10^4$. We therefore use $10^4 \times 10^5 = 10^9 \to \bar{A}_{\text{syst}}$ in Eq. (E4), leading the dashed line, in good agreement with simulation data, except for the two last points at high $C$. Solid lines from top to bottom correspond to Eq. (E4) with $\bar{A}_{\text{syst}} = 10^4$, $10^8$, $10^{16}$, $10^{32}$. (b) Probability $Q_{\text{trans}}$ as a function of $C$. From right to left (or top to bottom), we have $\bar{A}_{\text{syst}} = 10^{2+n}$ with $n = 0, \dots, 6$, and $10^{16}$, $10^{32}$. (c) Transition threshold $C_c$ as a function of $\bar{A}_{\text{syst}}$. Red squares: simulation results; blue dots: analytical model; black diamonds: solution of the equation $P_{\text{av}} = 1/2$. Dashed lines are guides to the eye: from top to bottom $0.58x^{-0.028}$, $0.38x^{-0.032}$, and $0.31x^{-0.0335}$.

The last equality is obtained using integration by parts in the limit $C_{\max} \gg C_c$. The numerical estimate of $C_c$ is not sensitive to the precise choice of $C_{\max}$ as long as $C_{\max} \gg C_c$.

The predicted value of $C_c$ is reported in Fig. 17(c). We find that the predicted transition is quantitatively lower than that observed in direct simulations in the range $A_{syst} \leqslant 10^8$. In addition, the decrease of $C_c$ with increasing $A_{syst}$ in simulations is slower than in the analytical model.

As an interesting result reported in Fig. 17(c), the average value of the transition can be recovered by the condition $P_{av} = 1/2$. Hence, within our model, the transition is mainly controlled by the possibility for a macroscopic avalanche to spread through the whole system rather than being controlled by the details of the initial growth dynamics of the avalanche (described by $P_{start}$). Note that $P_{start}$ is by far the most difficult quantity to evaluate.

[1] R. Livi and P. Politi, *Nonequilibrium Statistical Physics: A Modern Perspective* (Cambridge University Press, Cambridge, 2017).

[2] P. L. Krapivsky, S. Redner, and E. Ben-Naim, *A Kinetic View of Statistical Physics* (Cambridge University Press, Cambridge, 2010).

[3] M. Aizenman and J. L. Lebowitz, Metastability effects in bootstrap percolation, J. Phys. A: Math. Gen. **21**, 3801 (1988).

[4] J. Adler, Bootstrap percolation, Physica A **171**, 453 (1991).

[5] P. De Gregorio, A. Lawlor, and K. A. Dawson, Bootstrap percolation, in *Complex Media and Percolation Theory*, edited by M. Sahimi and A. G. Hunt (Springer, New York, 2021), pp. 149–173.

[6] A. E. Holroyd, Sharp metastability threshold for two-dimensional bootstrap percolation, Probab. Theory Relat. Fields **125**, 195 (2003).

[7] P. De Gregorio, A. Lawlor, P. Bradley, and K. A. Dawson, Exact solution of a jamming transition: Closed equations for a bootstrap percolation problem, Proc. Natl. Acad. Sci. **102**, 5669 (2005).

[8] S. Manna, Abelian cascade dynamics in bootstrap percolation, Physica A **261**, 351 (1998).

[9] C. Farrow, P. M. Duxbury, and C. F. Moukarzel, Culling avalanches in bootstrap percolation, Phys. Rev. E **72**, 066109 (2005).

[10] C. L. Farrow, P. Shukla, and P. M. Duxbury, Dynamics of k-core percolation, J. Phys. A: Math. Theor. **40**, F581 (2007).

[11] R. M. D'Souza and J. Nagler, Anomalous critical and super-critical phenomena in explosive percolation, Nat. Phys. **11**, 531 (2015).

[12] R. M. D'Souza, J. Gómez-Gardenes, J. Nagler, and A. Arenas, Explosive phenomena in complex networks, Adv. Phys. **68**, 123 (2019).

[13] J. P. Sethna, K. Dahmen, S. Kartha, J. A. Krumhansl, B. W. Roberts, and J. D. Shore, Hysteresis and hierarchies: Dynamics of disorder-driven first-order phase transformations, Phys. Rev. Lett. **70**, 3347 (1993).

[14] M. L. Rosinberg, E. Kierlik, and G. Tarjus, Percolation, depinning, and avalanches in capillary condensation of gases in disordered porous solids, Europhys. Lett. **62**, 377 (2003).

[15] S. K. Nandi, G. Biroli, and G. Tarjus, Spinodals with disorder: From avalanches in random magnets to glassy dynamics, Phys. Rev. Lett. **116**, 145701 (2016).

[16] Y. Saito, *Statistical Physics of Crystal Growth* (World Scientific, Singapore, 1996).

[17] A. Paterson, M. Fermigier, P. Jenffer, and L. Limat, Wetting on heterogeneous surfaces: Experiments in an imperfect hele-shaw cell, Phys. Rev. E **51**, 1291 (1995).

[18] V. K. Horváth, F. Family, and T. Vicsek, Dynamic scaling of the interface in two-phase viscous flows in porous media, J. Phys. A: Math. Gen. **24**, L25 (1991).

[19] M. A. Rubio, C. A. Edwards, A. Dougherty, and J. P. Gollub, Self-affine fractal interfaces from immiscible displacement in porous media, Phys. Rev. Lett. **63**, 1685 (1989).

[20] A. Lii-Rosales, Y. Han, S. E. Julien, O. Pierre-Louis, D. Jing, K.-T. Wan, M. C. Tringides, J. W. Evans, and P. A. Thiel, Shapes of Fe nanocrystals encapsulated at the graphite surface, New J. Phys. **22**, 023016 (2020).

[21] Z. Zong, C.-L. Chen, M. R. Dokmeci, and K.-t. Wan, Direct measurement of graphene adhesion on silicon surface by intercalation of nanoparticles, J. Appl. Phys. **107**, 026104 (2010).

[22] J. Wang, D. C. Sorescu, S. Jeon, A. Belianinov, S. V. Kalinin, A. P. Baddorf, and P. Maksymovych, Atomic intercalation to measure adhesion of graphene on graphite, Nat. Commun. **7**, 1 (2016).

[23] M. Yamamoto, O. Pierre-Louis, J. Huang, M. S. Fuhrer, T. L. Einstein, and W. G. Cullen, The Princess and the Pea at the nanoscale: Wrinkling and delamination of graphene on nanoparticles, Phys. Rev. X **2**, 041018 (2012).

[24] M. Guedda, N. Alaa, and M. Benlahsen, Analytical results for the wrinkling of graphene on nanoparticles, Phys. Rev. E **94**, 042806 (2016).

[25] K. Zhang and M. Arroyo, Understanding and strain-engineering wrinkle networks in supported graphene through simulations, J. Mech. Phys. Solids **72**, 61 (2014).

[26] V. M. Pereira, A. H. Castro Neto, H. Y. Liang, and L. Mahadevan, Geometry, mechanics, and electronics of singular structures and wrinkles in graphene, Phys. Rev. Lett. **105**, 156603 (2010).

[27] D. Mollison, The rate of spatial propagation of simple epidemics, in *Proceedings of the Sixth Berkeley Symposium on Mathematical Statistics and Probability, Volume 3: Probability Theory* (University of California Press, Berkeley, 1972), pp. 579–614.

[28] M. Kuperman and H. Wio, Front propagation in epidemiological models with spatial dependence, Physica A **272**, 206 (1999).

[29] G. Abramson, V. Kenkre, T. Yates, and R. Parmenter, Traveling waves of infection in the hantavirus epidemics, Bull. Math. Biol. **65**, 519 (2003).

[30] E. Hanert, E. Schumacher, and E. Deleersnijder, Front dynamics in fractional-order epidemic models, J. Theor. Biol. **279**, 9 (2011).

[31] A. Ben-Israel and Y. Levin, The geometry of linear separability in data sets, Linear Algebra Appl. **416**, 75 (2006).

[32] A. Hardy, On the number of clusters, Comput. Stat. Data Anal. **23**, 83 (1996).

[33] A. José-García and W. Gómez-Flores, Automatic clustering using nature-inspired metaheuristics: A survey, Appl. Soft Comput. **41**, 192 (2016).

[34] D. Elizondo, The linear separability problem: Some testing methods, IEEE Tran. Neural Netw. **17**, 330 (2006).

[35] I. Steinwart and A. Christmann, *Support Vector Machines* (Springer, New York, 2008).

[36] L. Wang, *Support Vector Machines: Theory and Applications*, Studies in Fuzziness and Soft Computing Vol. 177 (Springer, New York, 2005).

[37] M. Jayaram and H. Fleyeh, Convex hulls in image processing: a scoping review, Am. J. Intell. Syst, **6**, 48 (2016).

[38] R. Malladi and J. A. Sethian, Image processing via level set curvature flow, Proc. Natl. Acad. Sci. USA **92**, 7046 (1995).

[39] R. Malladi and J. A. Sethian, Image processing: Flows under min/max curvature and mean curvature, Graph. Models Image Process. **58**, 127 (1996).

[40] E. T. Gawlinski and H. E. Stanley, Continuum percolation in two dimensions: Monte Carlo tests of scaling and universality for non-interacting discs, J. Phys. A: Math. Gen. **14**, L291 (1981).

[41] J. Quintanilla, S. Torquato, and R. M. Ziff, Efficient measurement of the percolation threshold for fully penetrable discs, J. Phys. A: Math. Gen. **33**, L399 (2000).

[42] R. Jarvis, On the identification of the convex hull of a finite set of points in the plane, Inf. Process. Lett. **2**, 18 (1973).

[43] D. Stauffer and A. Aharony, *Introduction to Percolation Theory* (Taylor & Francis, Oxford, 2018).

[44] J. Chalupa, P. L. Leath, and G. R. Reich, Bootstrap percolation on a Bethe lattice, J. Phys. C **12**, L31 (1979).

[45] J. Adler and A. Aharony, Diffusion percolation. I. Infinite time limit and bootstrap percolation, J. Phys. A: Math. Gen. **21**, 1387 (1988).

[46] S. N. Dorogovtsev, A. V. Goltsev, and J. F. F. Mendes, $k$-core organization of complex networks, Phys. Rev. Lett. **96**, 040601 (2006).

[47] M. A. Di Muro, L. D. Valdez, H. E. Stanley, S. V. Buldyrev, and L. A. Braunstein, Insights into bootstrap percolation: Its equivalence with $k$-core percolation and the giant component, Phys. Rev. E **99**, 022311 (2019).

[48] R. Lenormand and C. Zarcone, Growth of clusters during imbibition in a network of capillaries, in *Kinetics of Aggregation and Gelation*, edited by F. Family and D. P. Landau (Elsevier, Amsterdam, 1984), p. 177.

[49] J. Adler, D. Stauffer, and A. Aharony, Comparison of bootstrap percolation models, J. Phys. A: Math. Gen. **22**, L297 (1989).

[50] E. Schwerin, Über Spannungen und Formänderungen kreisringförmiger Membranen, Z. Angew. Math. Mech. **9**, 482 (1929).

[51] U. Komaragiri, M. Begley, and J. Simmonds, The mechanical response of freestanding circular elastic films under point and pressure loads, J. Appl. Mech. **72**, 203 (2005).